JEM Journal of Experimental Medicine

ARTICLE

Piezo1 channels restrain ILC2s and regulate the development of airway hyperreactivity

Benjamin P. Hurrell[1], Stephen Shen[1], Xin Li[1], Yoshihiro Sakano[1], Mohammad Hossein Kazemi[1], Christine Quach[1], Pedram Shafiei-Jahani[1], Kei Sakano[1], Homayon Ghiasi[2], and Omid Akbari[1]

Mechanosensitive ion channels sense force and pressure in immune cells to drive the inflammatory response in highly mechanical organs. Here, we report that Piezo1 channels repress group 2 innate lymphoid cell (ILC2)–driven type 2 inflammation in the lungs. Piezo1 is induced on lung ILC2s upon activation, as genetic ablation of Piezo1 in ILC2s increases their function and exacerbates the development of airway hyperreactivity (AHR). Conversely, Piezo1 agonist Yoda1 reduces ILC2-driven lung inflammation. Mechanistically, Yoda1 inhibits ILC2 cytokine secretion and proliferation in a KLF2-dependent manner, as we found that Piezo1 engagement reduces ILC2 oxidative metabolism. Consequently, in vivo Yoda1 treatment reduces the development of AHR in experimental models of ILC2-driven allergic asthma. Human-circulating ILC2s express and induce Piezo1 upon activation, as Yoda1 treatment of humanized mice reduces human ILC2-driven AHR. Our studies define Piezo1 as a critical regulator of ILC2s, and we propose the potential of Piezo1 activation as a novel therapeutic approach for the treatment of ILC2-driven allergic asthma.

Introduction

Immune cells encounter complex mechanical cues during activation. They convert mechanical alterations to electrochemical signals via the process of mechanosensation, as mechanosensitive ion channels (MSCs) have been increasingly recognized in the past decade to be the most important mechanism used by immune cells to sense the local microenvironment (Jaalouk and Lammerding, 2009; Cahalan et al., 2015; Coste et al., 2010). Mechanical stimuli activate MSCs allowing for the rapid influx of ions including Ca^{2+}, leading to cell membrane depolarization and downstream signaling pathways affecting cell homeostasis and gene expression (Coste et al., 2010; Saotome et al., 2018). These processes are tightly regulated, as dysfunction in mechanotransduction may lead to pathological conditions such as perturbations in body iron metabolism (Ma et al., 2021). The major families of MSCs include epithelial sodium channel/degenerin (ENaC/DEG) (Hanukoglu and Hanukoglu, 2016), Piezo channels (Coste et al., 2010), two-pore domain potassium (K2P) (Lesage and Lazdunski, 2000), transient receptor potential (TRP) (Samanta et al., 2018), and the transmembrane channel-like 1/2 (TMC1/2) (Kim et al., 2013), as they were all shown to play vital roles in pathological responses (Jia et al., 2020). Due to the largely mechanical nature of the lungs, accumulating evidence suggests that MSCs may play a pivotal role in pulmonary immune cell homeostasis (Jia et al., 2022). MSCs expressed in the lungs are naturally activated by mechanical forces and play key roles in both lung homeostasis and inflammation, as evidence suggests that dysfunction in mechanotransduction contributes to lung inflammation (Weber et al., 2020; Jia et al., 2022).

The recent discovery of Piezo channels has gathered strong interest in the field of immunology (Coste et al., 2010). They are ubiquitously expressed in mammalian cells and are opened by mechanical stimulation to allow the influx of Ca^{2+} into cells (Zhang et al., 2019). Piezo1 channels are highly expressed in the lungs—in particular in endothelial and epithelial cells (Friedrich et al., 2019; Diem et al., 2020), smooth muscle cells (Retailleau et al., 2015), macrophages, and monocytes (Solis et al., 2019—whereas Piezo2, mainly located in sensory tissues, can be found in airway innervating sensory neurons (Woo et al., 2015; Nonomura et al., 2018). Several studies highlight a crucial role for Piezo1 in both innate and adaptive immune cells. Piezo1 is crucial in the regulation of macrophage function and polarization and is involved in several diseases including Alzheimer's disease and atherosclerosis (Tang et al., 2023). Furthermore, Piezo1 activation was shown to be central in bacterial clearance (Geng et al., 2021). In the lungs, reports have shown that Piezo1

[1]Department of Molecular Microbiology and Immunology, Keck School of Medicine, University of Southern California, Los Angeles, CA, USA; [2]Department of Surgery, Center for Neurobiology and Vaccine Development, Ophthalmology Research, Cedars-Sinai Burns and Allen Research Institute, Los Angeles, CA, USA.

Correspondence to Omid Akbari: akbari@usc.edu.

activation in macrophages and monocytes contributes to lung inflammation (Solis et al., 2019), as Piezo1 activation enhances CXCL2 secretion in monocytes (Sato et al., 2020). Recently, Piezo1 was also shown to potentially control dendritic cell (DC) metabolism and function (Chakraborty et al., 2021), as Piezo1 activation on DCs further contributes to the differentiation of T cells in cancer (Wang et al., 2022). Interestingly, however, recent reports show that Piezo1 activation may negatively regulate T cell expansion (Jairaman et al., 2021). In an autoimmune neuroinflammation model, Piezo1 deletion in T cells enhanced regulatory T cell expansion, favoring the attenuation of the disease. Interestingly other reports suggest that Piezo1 activation may inhibit cell proliferation (Caulier et al., 2020; Yoneda et al., 2019). The results from these studies therefore suggest a crucial but complex and most probably tissue/cell-dependent role of Piezo1 in the regulation of immune cells.

Group 2 innate lymphoid cells (ILC2) induce airway inflammation independently of the adaptive immune system (Vivier et al., 2018; Spits and Mjösberg, 2022). They are the dominant ILC population in the lungs at steady state and share features of both innate and adaptive immune cells (Asaoka et al., 2022). Like innate cells, ILC2s rapidly detect danger by sensing alarmins including IL-25, IL-33, and thymic stromal lymphopoietin (TSLP), which leads to their rapid activation and expansion (Hurrell et al., 2018). Similar to T cells, however, ILC2s release type-2 cytokines including IL-5 and IL-13 that directly promote cardinal features of asthma, including eosinophil recruitment to the airways and the subsequent development of airway hyperreactivity (AHR). ILC2s are a dynamic population in the lungs, as we and others have previously shown that modulating their activation can have a direct impact on the pathology of lung inflammation (Hurrell et al., 2018). Although multiple exogenous factors were described to modulate ILC2 function, several reports suggest the role of cation channels in the intrinsic regulation of ILC2 activation. Recently, transient receptor potential cation channel subfamily M member 8 (TRPM8) was shown to modulate skin ILC2 activation (Xu et al., 2022), as we have recently described the vital role of Orai channels on ILC2 function (Howard et al., 2023). However, the potential presence of MSCs on ILC2s and the role of mechanotransduction in diseases driven by ILC2s such as asthma are unknown and remain to be elucidated.

In this study, we found for the first time the crucial role of Piezo1 channels on ILC2 function and development of AHR. While we found that naïve pulmonary ILC2s express low basal levels of Piezo1, these levels are efficiently induced by activation with IL-33. We importantly found that ILC2s lacking Piezo1 are more activated, showing, in particular, an upregulated oxidative phosphorylation (OXPHOS) signature associated with greater oxygen consumption rates (OCRs) ex vivo. As a result, *Il7r*^{cre}*Piezo1*$^{fl/fl}$ mice develop more severe AHR associated with an exacerbated inflammatory response, as we confirmed these effects are ILC2-driven in a series of adoptive transfer experiments. Conversely, we found that Piezo1 activation with selective agonist Yoda1 reduces ILC2 function both ex vivo and in vivo in response to IL-33 stimulation, significantly limiting the development of AHR and lung inflammation in models of ILC2-dependent airway inflammation. Mechanistically, Piezo1 activation induces transcription factor Kruppel-like factor (KLF) 2, leading to a reduction in NF-κB p65. Notably, suberanilohydroxamic acid (SAHA)—a specific KLF2 activator—reduces ILC2 function and inhibits OXPHOS in ILC2s ex vivo. Finally, we confirmed our findings in ILC2s isolated from human peripheral blood mononuclear cells (PBMCs). Together, our study identifies a novel regulator of ILC2 function and opens avenues for potential downstream mechanisms that may be pharmacologically manipulated to improve therapies for allergic asthma.

Results

Piezo1 is inducible in pulmonary ILC2s

Piezo1 plays a physiological role in tissues including the lungs, and pivotal cell-specific functions for Piezo1 are emerging in immune cells. Piezo1 deletion is embryonically lethal, suggesting a central role of Piezo1 not only in cell function but also in development (Li et al., 2014). We therefore first analyzed the single-cell transcriptome of pure populations of FACS-sorted ILC2s isolated from the lungs of PBS-challenged mice or mice intranasally (i.n.) challenged on 3 consecutive days with IL-33, focusing on Piezo1-encoding gene *Piezo1* (Wallrapp et al., 2017) (Fig. 1 A). We found that although a very low number of scattered cells (0.2%) express *Piezo1* at steady state (PBS), a clear upregulation of cells expressing *Piezo1* is induced by IL-33 activation in ILC2s (Fig. 1 A, right panels). Of note, <1% of total IL-33–activated ILC2s express *Piezo2* (data not shown), whereas 61.2% of activated ILC2s express *Piezo1* in the inflamed lungs (Fig. 1 B and Fig. S2 H). Although other MSCs were detected in the analysis—including members of the TRP, ENaC/DEG, TREK, and TEMEM families—*Piezo1* is by far the most induced by activation, representing a log2 7.3-fold change compared with PBS controls (Fig. 1 C). IL-33 treatment induces the upregulation of ILC2 activation markers (Wallrapp et al., 2017). In particular, cytokines including *Il5*, *Il6*, *Il13*, and *Csf2*, proliferation markers including *Pcna*, *Mki67*, and *Cdk1* as well as ILC2 activation markers *Ilrl1*, *Areg*, and *Ahr* were all upregulated with IL-33 (Fig. 1 D). We next assessed the expression of these 10 transcripts relative to *Piezo1* (Fig. 1 E) and strikingly found that all were significantly enriched in the Piezo1^{low} population of activated ILC2s (Fig. 1 F). To analyze the dynamics of Piezo1 expression at the protein level, we next used mice expressing a fluorescent tdTomato reporter from the *Piezo1* promoter (Piezo1dT). Pure populations of FACS-sorted naïve lung ILC2s were cultured ex vivo in the presence of activation cytokine IL-33 or PBS for 24, 48, and 72 h (Fig. 1 G). Lung ILC2s were gated as live CD45$^+$, Lineage$^-$, CD127$^+$, and ST2$^+$ cells, expressing high levels of transcription factor GATA-3 (Fig. S1 A). Although we detected low basal levels of Piezo1 in PBS-treated ILC2s at all analyzed time points, activation with IL-33 progressively induced the expression of Piezo1 over time, reaching the highest levels after 72 h of activation (Fig. 1 H). Of note, we did not detect an upregulation of Piezo1 after 24 h of activation, as low protein levels only appeared after 48 h of culture with IL-33. To confirm our findings in an in vivo setting, cohorts of Piezo1dT mice were challenged i.n. on 3 consecutive days with IL-33 or vehicle, and on day 4, the expression of Piezo1 was measured by flow

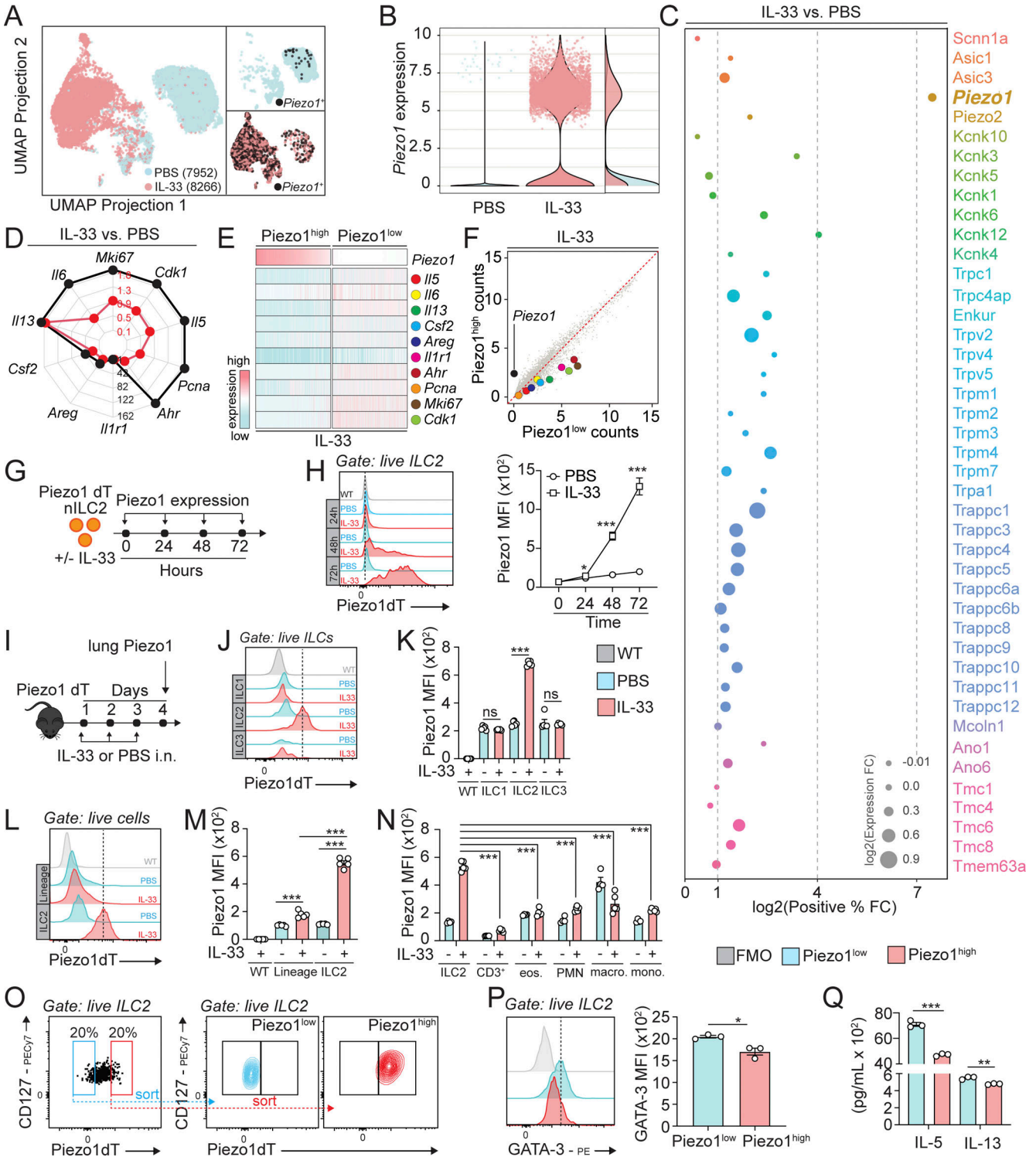

Figure 1. **ILC2 activation induces Piezo1 expression in the lungs. (A)** Pure populations of lung ILC2s were FACS-sorted from mice challenged with either PBS or IL-33 and profiled by droplet-based scRNA-seq (Wallrapp et al., 2017). Cells (dots) are colored based on in vivo treatment, either PBS (blue) or IL-33 (red). UMAP projections showing total ILC2s (left panel) and *Piezo1*⁺ ILC2s (right panel). **(B)** Corresponding quantitation of *Piezo1*⁺ ILC2s in PBS vs. IL-33–treated mice. Half violin plots represent overlaid density plots illustrating the distribution of *Piezo1* expression levels in each group. **(C)** *Piezo1*-positive % fold change (FC) relative to other known MSCs in IL-33–treated lung ILC2s, classified by group/color: red/orange: ENaC/ASIC; yellow: Piezo; green: TREK; blue: TRP; and pink/purple: TMEM16/Ano. **(D)** Radar plot depicting selected ILC2 signature activation genes induced by IL-33 treatment. Red dots represent log(fold change), and black dots represent $-\log_{10}$ (P value). **(E and F)** Heat map (E) and dot plot (F) representation of genes isolated in D in comparison to Piezo1^{high}- and Piezo1^{low}-expressing cells. **(G)** Schematic description of ex vivo lung ILC2 Piezo1 analysis. Pure populations of naïve ILC2s were FACS-sorted from the lungs of Piezo1dT mice and cultured ex vivo with rmIL-2 and rmIL-7 (both 10 ng/ml) for the indicated times with or without rmIL-33 (20 ng/ml). The experiment was performed twice. **(H)** Representative plots of Piezo1 expression at the indicated times and corresponding quantitation presented as Piezo1 mean fluorescence

intensity (MFI). *n* = 3. WT: C57BL/6 ILC2s. **(I)** Schematic description of in vivo lung immune cell Piezo1 analysis. Cohorts of Piezo1dT mice were challenged i.n. for 3 consecutive days with or without 0.5 µg rmIL-33, and on day 4, lung immune cells were analyzed by flow cytometry. The experiment was performed twice. **(J and K)** Representative plot of ILC1 (T-bet$^+$), ILC2 (GATA3$^+$), and ILC3 (RORgt$^+$) Piezo1 expression on day 4 (J) and corresponding quantitation presented as Piezo1dT MFI (K). *n* = 5. **(L and M)** Representative plot of Lineage$^+$ and ILC2 Piezo1 expression on day 4 (L) and corresponding quantitation presented as Piezo1dT MFI (M). *n* = 5. **(N)** Piezo1 expression in ILC2s, T cells (CD45$^+$CD3$^+$), eosinophils (CD45$^+$, CD11c$^-$, SiglecF$^+$), neutrophils (PMN, CD45$^+$, SiglecF$^-$, Ly6G$^+$, CD11b$^+$), macrophages (CD45$^+$, Ly6G$^-$, SiglecF$^-$, CD11c$^+$), and monocytes (CD45$^+$Ly6G$^-$, SiglecF$^-$Ly6C$^+$). *n* = 5. The experiment was performed twice. **(O–Q)** Piezo1dT mice were challenged i.n. for 3 consecutive days with rmIL-33 and pure populations of Piezo1dT-low–expressing (Piezo1^{low}, blue) and Piezo1dT-high–expressing (Piezo1^{high}, red) ILC2s were FACS-sorted on day 4 from the lungs for the indicated readouts. The experiment was performed twice. **(O)** Representative dot plots showing gating strategies for Piezo1^{high} and Piezo1^{low} populations and pure populations of Piezo1^{low} and Piezo1^{high} ILC2s. **(P)** Representative plots of intranuclear GATA-3 expression and corresponding quantitation were presented as GATA-3 MFI. *n* = 3. **(Q)** Pure populations of Piezo1^{low} and Piezo1^{high} ILC2s were further cultured ex vivo for 18 h with rmIL-2 and rmIL-7, and levels of IL-5 and IL-13 production in the culture supernatant were measured by ELISA. *n* = 3. Data are presented as mean ± SEM. A two-tailed Student's *t* test for unpaired data was applied for comparisons between two groups (H, K, M, P, and Q), except for multigroup comparisons where Tukey's multiple comparison one-way ANOVA tests were used (N). *P < 0.05, **P < 0.01, ***P < 0.001, ns: non-significant.

cytometry on lung ILC1, ILC2, and ILC3 (Fig. 1 I and Fig. S1 C). Confirming our ex vivo findings, naïve ILC2s expressed basal levels of Piezo1, as in vivo administration of IL-33 i.n. resulted in a significant upregulation of Piezo1 on ILC2s (Fig. 1, J and K). Of note, although ILC2s are the dominant ILC population found in the lungs in our setting, they expressed significantly more Piezo1 compared with ILC1 and ILC3 (Fig. 1, J and K). Interestingly, allergens and other ILC2 activators such as IL-25 and TSLP induced Piezo1 on ILC2s in vivo, albeit at a lower magnitude (Fig. S2, A–D). Expanding our analysis, we notably found that ILC2s not only express and induce Piezo1 but also represent the immune cell population with the highest levels of Piezo1 in our experimental setting, in particular in comparison with myeloid cells and T cells (Fig. 1, L–N). Together, our findings therefore suggest that Piezo1 is selectively upregulated at the transcriptomic and protein levels on activated pulmonary ILC2s.

Piezo1$^-$ and Piezo1$^+$ ILC2s are two functionally distinct populations of activated ILC2s

We next FACS-sorted and cultured pure populations of activated ILC2s either expressing low or high levels of Piezo1—respectively termed Piezo1^{low} and Piezo1^{high} ILC2s. Piezo1dT mice were challenged on 3 consecutive days with IL-33 i.n., and on day 4, lung ILC2s were sorted based on the expression of Piezo1 (20% low and 20% high), resulting in pure populations of either Piezo1^{low} and Piezo1^{high} ILC2s (Fig. 1 O). Interestingly, we first found that Piezo1^{high} ILC2s were slightly more viable compared with Piezo1^{low} ILC2s, suggesting that the expression of Piezo1 is not associated with cell death (Fig. S1 D). We further found that cultured Piezo1^{high} ILC2s expressed significantly less intranuclear GATA-3—the major transcription factor regulating ILC2 maintenance and function (Fig. 1 P). In confirmation of our transcriptomic analysis, ILC2s expressing high levels of Piezo1 secreted less effector cytokines, such as IL-5 and IL-13, in the culture supernatants (Fig. 1 Q). These findings therefore suggest that ILC2s expressing or not Piezo1 are functionally distinct, with Piezo1 expression surprisingly associated with lower markers of ILC2 activation, both at the transcriptomic and protein levels.

Piezo1-deficient ILC2s exhibit increased metabolic and functional activity

We next generated *Il7r^{cre}Piezo1$^{fl/fl}$* mice lacking *Piezo1* in ILC2s, a strategy previously used to study ILC2-dependent mechanisms in murine models (Halim et al., 2018) (Fig. S3). To measure the function of Piezo1 channels on ILC2s, control *Il7r^{cre}* and *Il7r^{cre}Piezo1$^{fl/fl}$* mice were challenged i.n. on 3 consecutive days with IL-33, and pure populations of lung ILC2s were cultured ex vivo for 18 h. Notably, we found that the absence of Piezo1 in ILC2s increased the levels of IL-5, IL-6, and IL-13 secretion compared with controls in the culture supernatants (Fig. 2 A). This phenotype was remarkably associated with an upregulation of intranuclear GATA-3 (Fig. 2 B). To understand how Piezo1 controls the molecular properties of ILC2s, we next performed a comprehensive transcriptomic analysis of pure populations of activated ILC2s isolated from *Il7r^{cre}* and *Il7r^{cre}Piezo1$^{fl/fl}$* mice (Fig. 2 C). As evidenced by the principal component analysis (PCA), the lack of *Piezo1* in ILC2s induced a distinct transcriptional profile compared with controls (Fig. 2 D). The differential analysis between the two groups identified that the lack of *Piezo1* induced the differential regulation of 586 genes (Fig. 2 E), as the top enriched pathways induced by the lack of *Piezo1* were associated with ILC2 activation and function (Fig. 2 F). In particular, ILC2 inflammation (Wallrapp et al., 2017), proliferation signature (Wallrapp et al., 2017), and Th2 pathways were all significantly upregulated. As expected, *Piezo1* expression was significantly downregulated—importantly resulting in a lack of expression at the protein level—as ILC2 signature cytokines *Il4*, *Il5*, *Il9*, *Il10*, and *Il13* were all significantly upregulated (Fig. 2, F and G; and Fig. S3 B). Mechanistically, the ERK/MAPK pathway involved in the regulation of ILC2 function (Petrova et al., 2020; Hurrell et al., 2022) was enriched in ILC2s lacking *Piezo1*, but more importantly, we found a net upregulation of genes associated with OXPHOS—the major source of ATP in ILC2s (Wilhelm et al., 2016)—suggesting that ILC2s lacking Piezo1 are metabolically more active. In particular, we found that the expression of major TCA cycle enzymes including *Aco1* and *Idh1* were upregulated by the lack of *Piezo1* in ILC2s (Fig. 2 H), a phenotype strongly associated with an increased mitochondrial activity gene signature (Fig. 2 I). We therefore next confirmed the central role of Piezo1 in ILC2 mitochondrial respiration by performing a series of bioenergetic assays (Fig. 2 J). In confirmation of our transcriptomic analysis, we found that basal respiration (Fig. 2 K), spare respiratory capacity (Fig. 2 L), and ATP production rates (Fig. 2 M) were all higher in *Il7r^{cre}Piezo1$^{fl/fl}$* compared with *Il7r^{cre}*-activated ILC2s. Together, our findings therefore indicate that Piezo1 may

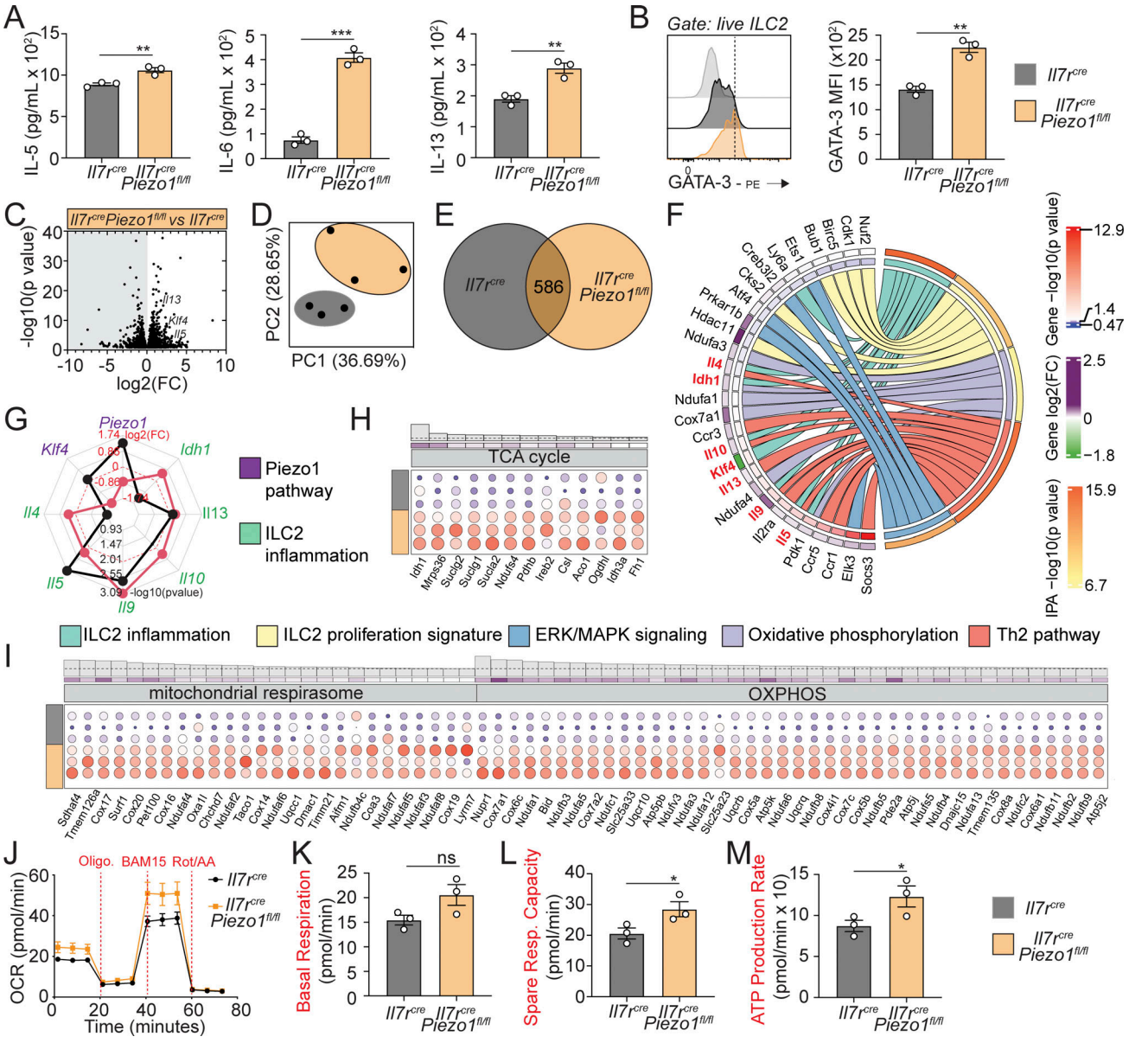

Figure 2. **ILC2s lacking *Piezo1* are metabolically and functionally more active.** *Il7r*^{cre} and *Il7r*^{cre}*Piezo1*$^{fl/fl}$ mice were challenged i.n. for 3 consecutive days with rmIL-33, and pure populations of lung ILC2s were isolated on day 4 and cultured with rmIL-2 and rmIL-7 for 18 h. Cells were then collected for the indicated readouts. **(A)** Levels of IL-5, IL-6, and IL-13 production in the culture supernatant. *n* = 3. The experiment was performed three times. **(B)** Representative plots of intranuclear GATA-3 expression and corresponding quantitation are presented as GATA-3 MFI. *n* = 3. The experiment was performed twice. **(C–H)** Cells were collected, and RNA was extracted to perform a bulk transcriptomic analysis. **(C)** Volcano plot comparison between *Il7r*^{cre} vs. *Il7r*^{cre}*Piezo1*$^{fl/fl}$. **(D)** PCA plot. **(E)** Venn diagram depicting the number of transcripts differentially modulated between *Il7r*^{cre} and *Il7r*^{cre}*Piezo1*$^{fl/fl}$ ILC2s differential analysis, with a statistical cutoff of P < 0.05. **(F)** Chord plot representing the highest differentially expressed genes (DEG) from the top five upregulated pathways. Specific pathways are color-coded and represented in the right inner bands, where chords gather. Outer bands on the right depict the IPA $-\log_{10}$ P value. The left inner bands represent the gene $-\log_{10}$ P value. Outer bands on the left represent the gene $\log_2$(fold change). **(G)** Radar plot depicting selected genes from the ILC2 inflammation and the Piezo1 pathway. Red dots represent log(fold change), and black dots represent $-\log_{10}$ (P value). **(H)** Differential expression of TCA cycle-related genes between *Il7r*^{cre} and *Il7r*^{cre}*Piezo1*$^{fl/fl}$ ILC2s. Gray histograms represent $-\log_{10}$ (P value), and the dotted line represents P < 0.05. Inner bands represent gene log(fold change). **(I)** Differential expression of genes between *Il7r*^{cre} and *Il7r*^{cre}*Piezo1*$^{fl/fl}$ ILC2s involved in the mitochondrial respirasome and OXPHOS. Gray histograms represent $-\log_{10}$ (P value), and the dotted line represents P < 0.05. Inner bands represent gene log(fold change). **(J–M)** Mitochondrial respiratory profile showing OCRs in response to oligomycin (ATP synthase inhibitor), BAM15 (mitochondrial uncoupler), and rotenone + antimycin A (complex I and II inhibitors) sequential injections (J) and corresponding key parameters of mitochondrial function (K) basal respiration, (L) spare respiratory capacity, and (M) ATP production rates. *n* = 3. The experiment was performed twice. Data are presented as mean ± SEM. A two-tailed Student's *t* test for unpaired data was applied for comparisons between two groups (A, B, and K–M). *P < 0.05, **P < 0.01, ***P < 0.001, and ns: non-significant.

restrain oxidative metabolism in ILC2s, ultimately controlling their activation and function.

The absence of Piezo1 in ILC2s exacerbates AHR and lung inflammation

To investigate the physiological role of Piezo1 in ILC2s, we induced a model of ILC2-driven AHR in *Il7r*^{cre} and *Il7r*^{cre}*Piezo1*$^{fl/fl}$ mice. Mice were challenged i.n. on days 1–3 with IL-33 and lung function as well as airway inflammation were measured on day 4 (Fig. 3 A). Compared with PBS-treated mice who did not receive IL-33, we first found that *Il7r*^{cre} control mice treated with IL-33 i.n. induced significantly higher lung resistance in response to increasing doses of bronchoconstrictor methacholine (Fig. 3 B). However, strikingly, *Il7r*^{cre}*Piezo1*$^{fl/fl}$ mice treated with IL-33 developed significantly more lung resistance compared with *Il7r*^{cre} controls. As a measure of lung elasticity, we further found that the dynamic compliance observed in *Il7r*^{cre}*Piezo1*$^{fl/fl}$ mice was reduced as compared with *Il7r*^{cre} controls (Fig. 3 C). In line with these findings, the number of ILC2s per lung was increased in *Il7r*^{cre}*Piezo1*$^{fl/fl}$ mice (Fig. 3 D). To better characterize the function of Piezo1 on ILC2s in vivo, we next measured survival, proliferation, and activation markers on lung ILC2s following 3 days of IL-33 i.n. challenge. Although we did not find differences in apoptosis (Fig. 3 E), we found that ILC2s isolated from the lungs of *Il7r*^{cre}*Piezo1*$^{fl/fl}$ mice expressed significantly more intranuclear proliferation marker Ki67 (Fig. 3 F) and activation marker GATA-3 (Fig. 3 G), suggesting an increased activation in the absence of Piezo1. As expected, the number of CD45^{+} cells found in the bronchoalveolar lavage (BAL) was higher in *Il7r*^{cre}*Piezo1*$^{fl/fl}$ mice compared with controls (Fig. 3 H), representing in particular an increase in eosinophils (Fig. 3 I and Fig. S1 B). Overall our findings indicate an increase in ILC2-driven airway inflammation in *Il7r*^{cre}*Piezo1*$^{fl/fl}$ mice (Fig. 3 J), associated with increased airway epithelial thickness compared with controls (Fig. 3 K). Because IL7Rα^{cre}-driven deletion may not be entirely ILC2 specific (Halim et al., 2018) and to exclude any bystander effects, we next measured airway inflammation in alymphoid mice adoptively transferred with *Il7r*^{cre} or *Il7r*^{cre}*Piezo1*$^{fl/fl}$ activated ILC2s and challenged for a further 3 days i.n. with IL-33 (Fig. 3 L). We first found that mice adoptively transferred with control ILC2s developed significantly more lung resistance compared with non-transferred controls (Fig. 3 M). In confirmation of our previous findings, however, mice adoptively transferred with *Il7r*^{cre}*Piezo1*$^{fl/fl}$ ILC2s developed higher lung resistance compared with control mice who received *Il7r*^{cre} ILC2s (Fig. 3 M). The observed phenotype was associated with increased lung ILC2s (Fig. 3 N) and a higher number of eosinophils in the BAL (Fig. 3 O). In summary, our ex vivo and in vivo findings combine to suggest that a lack of Piezo1 is associated with increased ILC2 function, in turn exacerbating the development of ILC2-dependent AHR and airway inflammation.

Piezo1 regulates ILC2 effector functions

Because a lack of Piezo1 increased ILC2 function, we next addressed whether Piezo1 activation could restrain ILC2s and therefore serve as a negative regulator of ILC2s. Yoda1 is a selective Piezo1 agonist leading to downstream effects on gene transcription in a multitude of cells (Syeda et al., 2015) (Fig. 4 A). We, therefore, cultured activated ILC2s with or without Yoda1 for 18 h and measured the effects of Piezo1 activation on ILC2 function (Fig. 4 B). Compared with controls, Yoda1-treated ILC2s secreted significantly lower effector cytokines including IL-5, IL-6, and IL-13 in the culture supernatants (Fig. 3 C), although we found similar ILC2 apoptotic rates suggesting that the treatment is not toxic to cells (Fig. 4 D). Furthermore, Piezo1 activation using Yoda1 ex vivo reduced intranuclear GATA-3 (Fig. 4 E) and Ki67 (Fig. 4 F) expressions in ILC2s. To confirm that the observed effects induced by Yoda1 were specific to Piezo1, we next performed a series of experiments on activated ILC2s isolated from *Il7r*^{cre}*Piezo1*$^{fl/fl}$ mice (Fig. 4 G). We cultured pure populations of activated ILC2s isolated from the lungs of *Il7r*^{cre}*Piezo1*$^{fl/fl}$ mice with or without Yoda1 and remarkably found no effect on cytokine secretion (Fig. 4 H). Additionally, Yoda1 did not modulate ILC2 proliferation, as evidenced by similar intranuclear Ki67 expression levels in the vehicle or Yoda1-treated *Il7r*^{cre}*Piezo1*$^{fl/fl}$ ILC2s (Fig. 4 I). To confirm our findings in vivo, BALB/c mice were challenged i.n. on 3 consecutive days with IL-33 and intraperitoneal injections of Yoda1 or vehicle (Fig. 4 J). We found that Piezo1 activation using Yoda1 reduced ILC2 numbers in the lungs compared with controls (Fig. 4 K) although it did not affect the viability of ILC2s (Fig. 4 L). In confirmation of our ex vivo findings, in vivo Yoda1 treatment reduced intranuclear GATA-3 (Fig. 4 M) and Ki67 (Fig. 4 N) expressions as well as the intracellular levels of IL-13 (Fig. 4, O and P) and IL-5 (Fig. 4, Q and R). Together, our findings using Yoda1 ex vivo and in vivo suggest that Piezo1 activation limits ILC2 function.

Piezo1 inhibits mitochondrial respiration and modulates ILC2 metabolic activity

To better characterize the effects of Piezo1 activation on the molecular properties of ILC2s, we next performed a transcriptomic analysis of pure populations of ILC2s cultured with or without Yoda1 for 18 h. As observed by the volcano plot and PCA, Yoda1 induced a distinct transcriptional profile compared with controls, with, in particular, a 28.82% PC1 variance index between the two groups (Fig. 5, A and B). Similar to our previous RNA sequencing (RNA-seq) analysis depicted in Fig. 2, the differential analysis between the two groups identified the regulation of 867 genes (Fig. 5 C), as an Ingenuity Pathway Analysis (IPA) analysis revealed that the top five enriched pathways were associated with an inhibition of ILC2 activation and proliferation gene signatures (Fig. 5 D). In particular, ILC2 inflammation (Wallrapp et al., 2017), ILC2 proliferation (Wallrapp et al., 2017), and Th2 pathways were significantly downregulated by Piezo1 activation, an observation in sharp contrast to our previous analysis using ILC2s lacking Piezo1 (Fig. 2 F). Mechanistically, we further found the downregulation of the ERK/MAPK signaling pathway and a strong inhibitory effect of Yoda1 treatment on ILC2 proliferation. Importantly, TCA cycle enzymes including *Cs*, *Idh2*, and *Aco2* were highly downregulated following Yoda1 treatment, as we further observed the downregulation of mitochondrial function and OXPHOS gene signatures in Yoda1-treated ILC2s (Fig. 5 E). We next performed bioenergetic

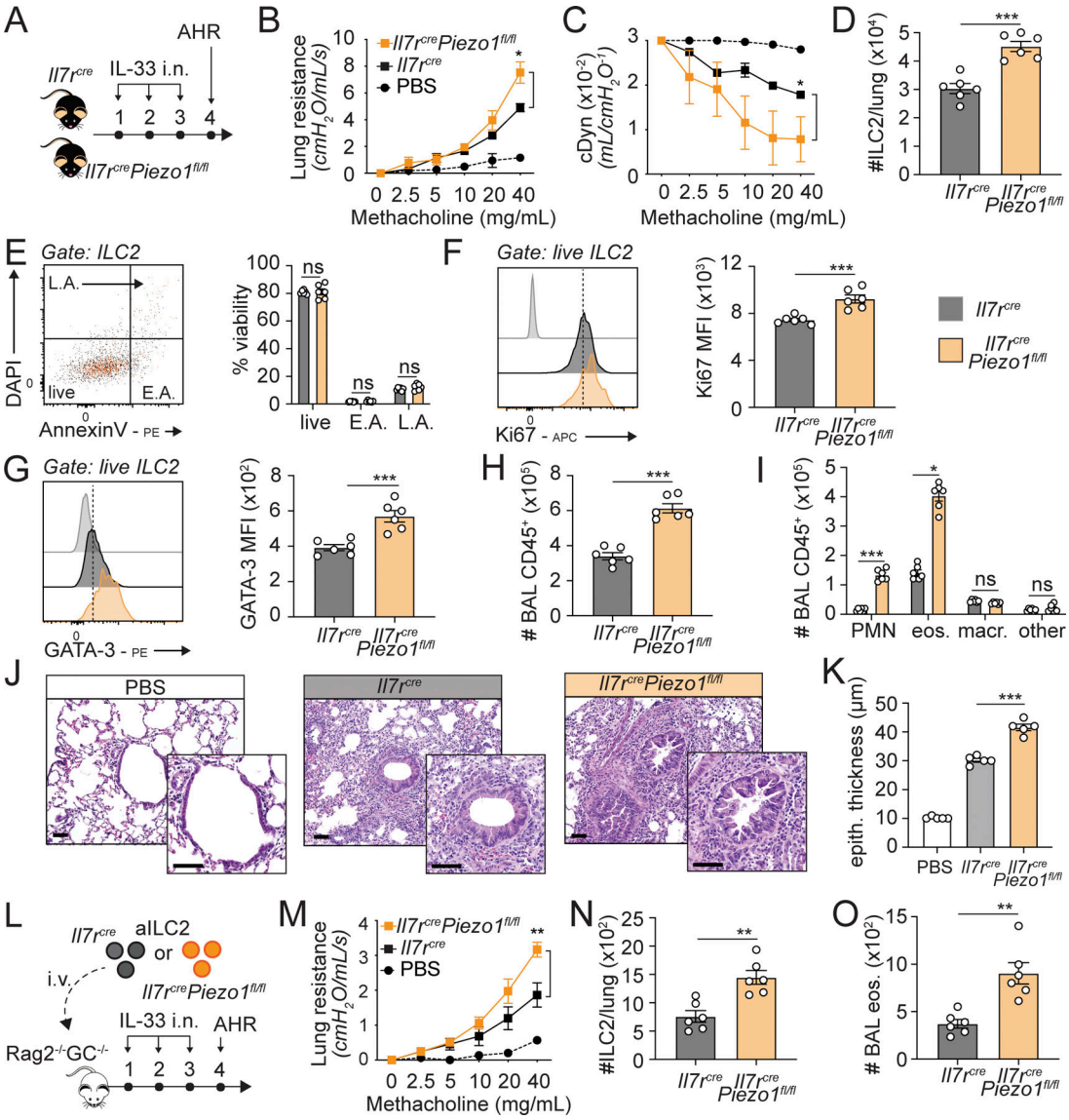

Figure 3. **Lack of Piezo1 in ILC2s increases AHR and lung inflammation. (A)** Schematic description of in vivo effects of Piezo1-deficient ILC2s on the development of AHR. *Il7r*^{cre} and *Il7r*^{cre}*Piezo1*$^{fl/fl}$ mice received 0.5 µg rmIL-33 or PBS i.n. on days 1–3. On day 4, lung function, lung ILC2s, BAL cellularity, and histology were analyzed. The experiment was performed twice. **(B and C)** Lung resistance (B) and dynamic compliance (C) in response to increasing doses of methacholine. *n* = 4. **(D)** Total number of ILC2s per lung. *n* = 6. **(E)** Representative plots of live, early apoptotic (E.A.), and late apoptotic/necrotic (L.A.) ILC2s and corresponding quantitation presented as the frequencies (%) of live, E.A., and L.A. ILC2s. *n* = 6. **(F and G)** Representative plots of intranuclear (F) Ki67 and (G) GATA-3 expressions and corresponding quantitations are presented as MFI. *n* = 6. **(H)** Total number of CD45$^+$ lymphoid cells in the BAL. *n* = 6. **(I)** Numbers of BAL eosinophils (CD45$^+$, CD11c$^-$, SiglecF$^+$), neutrophils (PMN, CD45$^+$, SiglecF$^-$, Ly6G$^+$, and CD11b$^+$), macrophages (CD45$^+$, Ly6G$^-$, SiglecF$^-$, and CD11c$^+$), and other. *n* = 6. **(J)** Lung histology. Scale bars, 50 µm. **(K)** Average alveolar epithelial thickness. *n* = 5. **(L)** Schematic representation of the induction of airway inflammation by adoptively transferred *Il7r*^{cre} or *Il7r*^{cre}*Piezo1*$^{fl/fl}$ ILC2s in alymphoid recipients. *Il7r*^{cre} and *Il7r*^{cre}*Piezo1*$^{fl/fl}$ mice were challenged i.n. on 3 consecutive days with rmIL-33, and pure populations of lung ILC2s were isolated on day 4. 5 × 10^4 Il7r^{cre} or *Il7r*^{cre}*Piezo1*$^{fl/fl}$ ILC2s were then subsequently transferred intravenously to *Rag*$^{-/-}$*GC*$^{-/-}$ recipient mice, who then received 0.5 µg rmIL-33 i.n. on days 1–3. On day 4, lung function, lung ILC2s, and BAL cellularity were analyzed. The experiment was performed three times. **(M)** Lung resistance in response to increasing doses of methacholine. *n* = 6. **(N)** Total number of ILC2s per lung. *n* = 6. **(O)** Total number of BAL eosinophils (CD45$^+$, CD11c$^-$, SiglecF$^+$). *n* = 6. Data are presented as mean ± SEM. A two-tailed Student's *t* test for unpaired data was applied for comparisons between two groups (D–I, N, and O), except for multigroup comparisons where Tukey's multiple comparison one-way ANOVA tests were used (B, C, K, and M). *P < 0.05, **P < 0.01, ***P < 0.001, and ns: non-significant.

assays to confirm the effects of Yoda1 on ILC2 metabolism, measuring OCRs in ILC2s treated or not with Yoda1 ex vivo (Fig. 5 F). We found that basal respiration (Fig. 5 G), spare respiratory capacity (Fig. 5 H), and ATP production rates (Fig. 5 I) were all reduced in Yoda1-treated ILC2s. Interestingly, this modulation of oxidative metabolism was associated with a net decrease in fatty acid metabolism gene signature—the major source fueling ILC2 oxidative metabolism (Fig. S4 A). Of note, Yoda1 also appeared to induce a glycolytic gene signature in ILC2s as a compensatory mechanism to generate ATP (Fig. S4 A). Together, our findings therefore indicate that Piezo1 activation inhibits mitochondrial respiration and modulates ILC2 oxidative metabolism.

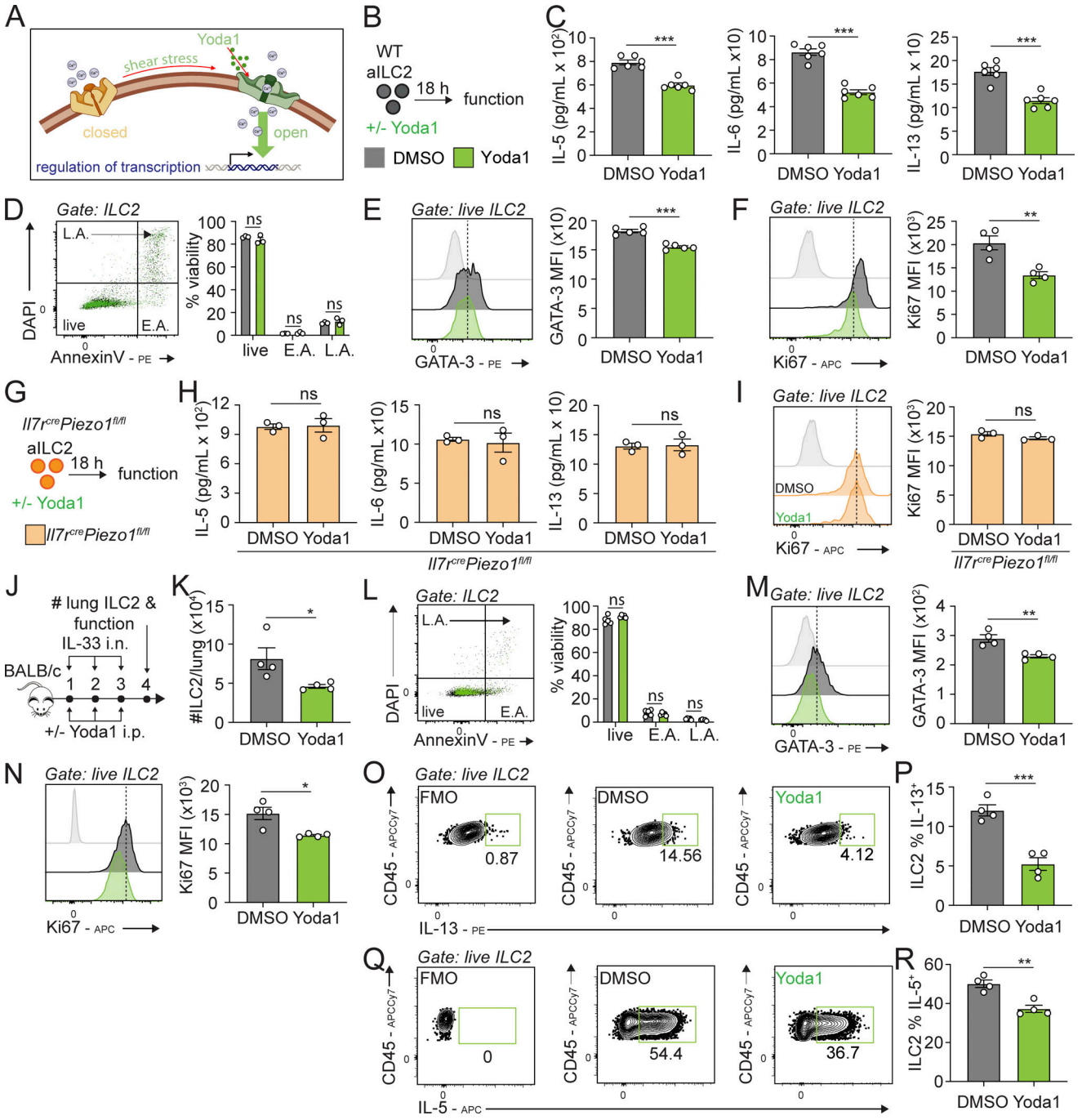

Figure 4. **Yoda1 limits ILC2 function ex vivo and in vivo in a Piezo1-dependent manner. (A)** Representative diagram detailing the activation of the Piezo1 channel by shear stress or agonistic activation by Yoda1 leading to an influx of cations, resulting in regulation of transcription. **(B)** Schematic description of ex vivo ILC2 Piezo1 activation. BALB/c mice were challenged i.n. for 3 consecutive days with rmIL-33, and a pure population of lung ILC2s was isolated on day 4 and cultured with rmIL-2, rmIL-7 with or without Yoda1 (10 µM) for 18 h. **(C)** Levels of IL-5, IL-6, and IL-13 production in the culture supernatant. *n* = 6. The experiment was performed three times. **(D)** Representative plots of live, early apoptotic (E.A.), and late apoptotic/necrotic (L.A.) ILC2s and corresponding quantitation presented as the frequencies (%) of live, E.A., and L.A. ILC2s. *n* = 3. The experiment was performed twice. **(E and F)** Representative plots of intranuclear (E) GATA-3 (*n* = 5) and (F) Ki67 (*n* = 4) expressions and corresponding quantitation are presented as MFI. The experiments were performed three times. **(G)** Schematic description of ex vivo ILC2 Piezo1 activation. *Il7r^cre Piezo1^fl/fl* mice were challenged i.n. for 3 consecutive days with rmIL-33, and a pure population of lung ILC2s was isolated on day 4 and cultured with rmIL-2, rmIL-7 with or without Yoda1 (10 µM) for 18 h. **(H)** Levels of IL-5, IL-6, and IL-13 production in the culture supernatant. *n* = 3. The experiment was performed twice. **(I)** Representative plots of intranuclear Ki67 expressions and corresponding quantitation are presented as MFI. *n* = 3. The experiment was performed twice. **(J)** Schematic description of in vivo effects of Piezo1 activation. BALB/c mice were challenged i.n. on 3 consecutive days with rmIL-33 and Yoda1 (213 µg/kg/day) or vehicle intraperitoneally. On day 4, lungs were collected and processed to single-cell suspensions for the selected readouts. The experiment was performed twice. **(K)** Numbers of ILC2s per lung. *n* = 4. **(L)** Representative plots of live, early apoptotic (E.A.), and late apoptotic/necrotic (L.A.) ILC2s and corresponding quantitation presented as the frequencies (%) of live, E.A., and L.A. ILC2s. *n* = 4. **(M and N)** Representative plots of intranuclear (M) GATA-3 and (N) Ki67 expressions and corresponding quantitation are presented as MFI. *n* = 4. **(O and**

P) Representative plots of levels of intracellular IL-13 (O) and (P) corresponding quantitation of IL-13–positive ILC2s from the vehicle or Yoda1-treated mice. *n* = 4. **(Q and R)** Representative plots of levels of intracellular IL-5 (O) and (R) corresponding quantitation of IL-5–positive ILC2s from the vehicle or Yoda1-treated mice. *n* = 4. Data are presented as mean ± SEM. A two-tailed Student's *t* test for unpaired data was applied for comparisons between two groups (C–F, H, I, K–N, P, and R). *P < 0.05, **P < 0.01, ***P < 0.001, and ns: non-significant.

Piezo1 engagement limits ILC2 activation through the induction of KLF2

Reports have shown that Piezo1 channels sense shear force to induce mechanosensitive transcription factors (MSTF) KLF2/4 via a CaMKII/MEKK3/ERK5 signaling cascade (Zheng et al., 2022). Among all MSTFs, KLF2 is the best characterized and has been the target of pharmacological-based approaches for diseases such as atherosclerosis (Niu et al., 2019; Dabravolski et al., 2022). Mechanistically, KLF2 inhibits the expression of proinflammatory genes via inhibition of the NF-κB pathway (Das et al., 2006), a pathway central to the ILC2 function (Fig. 5 J). Our transcriptomic analysis notably showed that Yoda1 treatment significantly induced *Klf2* as well as *Mef2b*—an essential component of KLF2 signaling (Liu et al., 2023a) (Fig. 5 K). Furthermore, we found a net reduction in *Nfkb1*—encoding NF-κB RelA p65—as well as notable NF-κB pathway genes and downstream targets (Fig. 5 K), suggesting that the KLF2–NF-κB axis may contribute to the observed effects of Yoda1 on ILC2s. We confirmed the effects of Yoda1 on the induction of KLF2 in ILC2s at the protein level (Fig. 5 L and Fig. S4 B) as it also reduced intranuclear levels of NF-κB p65 (Fig. 5 M). Of note, KLF2 expression was reduced in ILC2s lacking Piezo1, supporting the notion that Piezo1 acts in a KLF2-dependent manner (Fig. S3 D). We therefore tested the effects of KLF2 pharmacological inducer SAHA on pure populations of ILC2s cultured ex vivo for 18 h (Xu et al., 2017) (Fig. 5 N). Importantly, we tested the toxicity of increasing concentrations of SAHA ranging from 0.1 to 10 µM and did not find significant effects on ILC2 survival, even at the highest dose tested (Fig. S4 C). As expected, we found that SAHA induced KLF2 at the protein level (Fig. 5 O) and was associated with decreased intranuclear levels of NF-κB p65 (Fig. 5 P). We further found that SAHA reduced intranuclear GATA-3 (Fig. 5 Q) and Ki67 (Fig. 5 R) expressions. As a result, KLF2 activation reduced the secretion of ILC2 major cytokines IL-5 (Fig. 5 S), IL-6 (Fig. 5 T), and IL-13 (Fig. 5 U). Finally, treatment of ILC2s with SAHA affected ILC2 oxidative metabolism (Fig. 5 V), as we found that basal respiration (Fig. 5 W), spare respiratory capacity (Fig. 5 X), and ATP production rates (Fig. 5 Y) were all reduced in SAHA-treated ILC2s. Interestingly, in vivo treatment of mice with SAHA in combination with IL-33 i.n. challenge for 3 consecutive days affected both ILC2 function and proliferation (Fig. S4, D–F). Together, our studies have therefore identified KLF2 as a downstream regulator of Piezo1 activation in ILC2s as KLF2 induction is able to decrease ILC2 function and oxidative metabolism.

Administration of Yoda1 in mice alleviates AHR and lung inflammation

To investigate the physiological role of Piezo1 activation on ILC2s, we treated mice with Yoda1 in a model of ILC2-dependent AHR. Cohorts of BALB/c mice were treated or not with Yoda1 intraperitoneally and challenged on days 1–3 with IL-33 i.n. and lung function as well as airway inflammation were measured on day 4 (Fig. 6 A). As expected, PBS-treated mice do not induce airway resistance and were used as a technical control for the assay (Fig. 6 B). However, control mice challenged with IL-33 i.n. induced lung resistance in comparison with PBS-treated mice, which was significantly reduced upon treatment with Yoda1 (Fig. 6 B). Consequently, Yoda1-treated mice showed improved dynamic compliance—a measure of lung elasticity—compared with controls in response to IL-33 (Fig. 6 C). This reduced severity in AHR was associated with a decrease in lung ILC2 numbers (Fig. 6 D), and as expected a reduction in ILC2 signature cytokines IL-4, IL-5, IL-6, and IL-13 in the BAL supernatants (Fig. 6 E). Importantly, we found a reduction of total CD45$^+$ cells in the BAL—in particular eosinophils—indicative of a reduced ILC2-driven inflammation (Fig. 6, F and G). Histological analysis confirmed an overall reduction in lung inflammation (Fig. 6 H), associated with a decrease in epithelial thickness—a marker of lung remodeling during airway inflammation—in mice treated with Yoda1 (Fig. 6 I). We next confirmed that the observed effects were ILC2-specific and conducted a series of experiments in *Rag2*$^{-/-}$ mice who lack T and B cells (Fig. 6 J). Similar to our findings in WT mice, Yoda1-treated *Rag2*$^{-/-}$ mice showed reduced lung resistance (Fig. 6 K) and improved dynamic compliance (Fig. 6 L) compared with controls. We further confirmed a reduced ILC2-driven inflammation in Yoda1-treated mice compared with controls, in particular, with regard to lung ILC2 numbers (Fig. 6 M), ILC2 signature cytokines in the BAL (Fig. 6 N), and cellular infiltrates in the BAL, including eosinophils (Fig. 6, O and P). As expected, histology analysis of the lungs confirmed a reduced inflammation in mice who were challenged with Yoda1 (Fig. 6, Q and R). Together, our in vivo analysis confirms an inhibitory role of Yoda1 on ILC2-driven airway inflammation and AHR.

Yoda1 in vivo limits the development of *Alternaria alternata*–induced AHR

Chronic exposure to allergens, including dust, mold, or fungi, has been identified as a contributing factor to the onset of asthma. Notably, *A. alternata* has been identified as the principal allergen associated with asthma in American households (Salo et al., 2006). In murine models, intranasal exposure to *A. alternata* elicits the activation of ILC2s through the IL-33/ST2 pathway. This activation subsequently induces ILC2 proliferation, cytokine production, and the development of AHR. We therefore investigated the implications of in vivo Yoda1 challenge in a murine model of allergen-induced AHR using *A. alternata* (Fig. S5 A). We first found that intranasal administration of *A. alternata* on 4 consecutive days in WT mice induced Piezo1 expression in ILC2s (Fig. S2, A and B). In *Rag2*$^{-/-}$ mice, vehicle-treated mice induced lung resistance compared with PBS controls, and

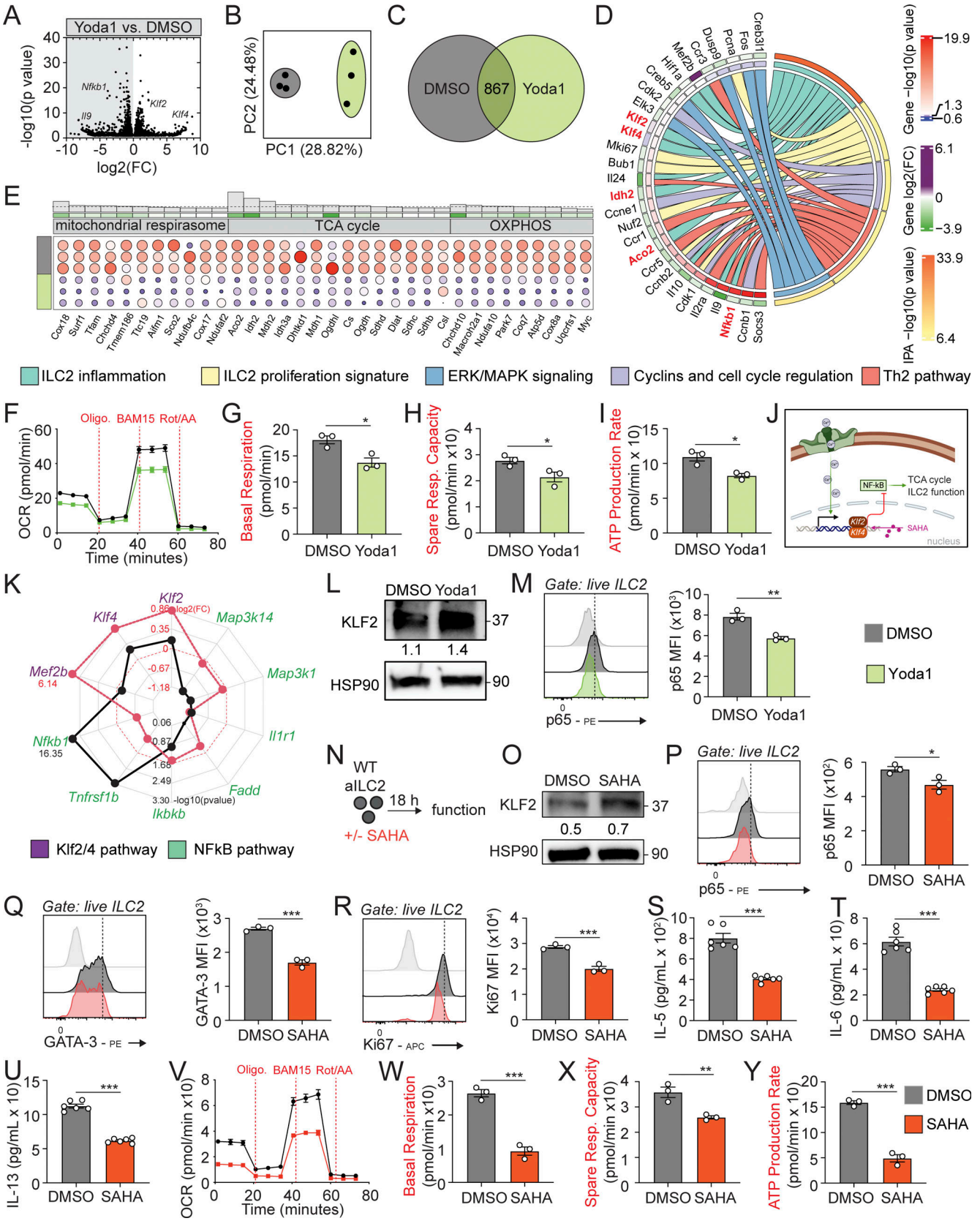

Figure 5. **Piezo1 activation and a KLF2 inducer inhibit mitochondrial respiration in ILC2s.** BALB/c mice were challenged i.n. on 3 consecutive days with rmIL-33, and a pure population of lung ILC2s was isolated on day 4 and cultured with rmIL-2, rmIL-7 without or with Yoda1 (10 µM) for 18 h. Cells were collected, and RNA was extracted to perform a bulk transcriptomic analysis. **(A)** Volcano plot comparison between DMSO-treated and Yoda1-treated ILC2s. **(B)** PCA plot. **(C)** Venn diagram depicting the number of transcripts differentially modulated between DMSO-treated and Yoda1-treated ILC2s differential

analysis, with a statistical cutoff of P < 0.05. **(D)** Chord plot representing the highest DEG from the top five downregulated pathways. Specific pathways are color-coded and represented in the right inner bands, where chords gather. Outer bands on the right depict the IPA $-\log_{10}$ P value. The left inner bands represent the gene $-\log_{10}$ P value. Outer bands on the left represent the gene $\log_2$(fold change). **(E)** Differential expression of genes between DMSO-treated and Yoda1-treated ILC2s involved in the mitochondrial respirasome, TCA cycle, and OXPHOS pathways. Gray histograms represent $-\log_{10}$ (P value); dotted line represents P < 0.05. Inner bands represent gene log(fold change). **(F–I)** Mitochondrial respiratory profile showing OCRs in response to oligomycin (ATP synthase inhibitor), BAM15 (mitochondrial uncoupler), and rotenone + antimycin A (complex I and II inhibitors) sequential injections (F) and corresponding key parameters of mitochondrial function (G) basal respiration, (H) spare respiratory capacity, and (I) ATP production rates. *n* = 3. The experiment was performed twice. **(J)** Representative diagram detailing the signaling of Piezo1 leading to downstream activation of KLF2/4 resulting in inhibition of the NF-κB pathway and downstream effects on TCA cycle and ILC2 function. **(K)** Radar plot depicting selected genes from the ILC2 inflammation and the KLF2/4 pathway. Red dots represent log(fold change), and black dots represent $-\log_{10}$ (P value). **(L)** Protein levels of KLF2 and HSP90 monitored by western blot and quantified with ImageJ. The experiment was performed twice. **(M)** Representative plots of intranuclear p65 expression and corresponding quantitation presented as MFI. *n* = 3. The experiment was performed twice. **(N)** Schematic description of ex vivo ILC2 incubation with SAHA. BALB/c mice were challenged i.n. for 3 consecutive days with rmIL-33, and pure populations of lung ILC2s were isolated and cultured on day 4 with rmIL-2, rmIL-7 with or without SAHA (1 µM) for 18 h. **(O)** Protein levels of KLF2 and HSP90 monitored by western blot and quantified with ImageJ. The experiment was performed twice. **(P–R)** Representative plots of intranuclear (P) p65, (Q) GATA-3, and (R) Ki67 expressions and corresponding quantitation presented as MFI. *n* = 3. These experiments were performed twice. **(S–U)** Levels of (S) IL-5, (T) IL-6, and (U) IL-13 production in the culture supernatant. *n* = 6. The experiment was performed twice. **(V–Y)** Mitochondrial respiratory profile showing OCRs in response to oligomycin (ATP synthase inhibitor), BAM15 (mitochondrial uncoupler), and rotenone + antimycin A (complex I and II inhibitors) sequential injections (V) and corresponding key parameters of mitochondrial function (W) basal respiration, (X) spare respiratory capacity, and (Y) ATP production rates. *n* = 3. The experiment was performed twice. Data are presented as mean ± SEM. A two-tailed Student's *t* test for unpaired data was applied for comparisons between two groups (G–I, M, P–U, and W–Y). *P < 0.05, **P < 0.01, ***P < 0.001. Source data are available for this figure: SourceData F5.

Yoda1 treatment reduced AHR compared to vehicle controls (Fig. S5, B and C). In support of our previous findings, Yoda1 further inhibited the ILC2 response compared with vehicle controls (Fig. S5, D–I). Collectively, these findings indicate that our observations, initially derived from the IL-33 model of airway inflammation, remain consistent when utilizing a more physiologically relevant and commonly employed allergen.

Piezo1 limits the effector function of human ILC2s and regulates oxidative metabolism

We next investigated the translational approach of our findings in human ILC2s isolated from PBMCs. Pure populations of hILC2s were therefore FACS-sorted and incubated for 72 h to (1) assess the expression of Piezo1 and (2) measure the effects of Yoda1 on ILC2 function (Fig. 7 A). hILC2s were gated as $CD45^+$, $Lineage^-$, $CD127^+$, and $CRTH2^+$ cells, and were FACS-sorted to a purity of >95% (Fig. 7 B). Based on the analysis of six healthy donors, we first found that hILC2s express Piezo1 at steady state, although IL-33 stimulation is able to induce this expression (Fig. 7, C and D). In support of our murine findings, we found that Yoda1 treatment consistently reduces the secretion of ILC2 effector cytokines IL-5, IL-6, and IL-13 in the culture supernatants (Fig. 7 E), as it also reduces the expression of major ILC2 regulator GATA-3 (Fig. 7 F). Consistent with our murine findings (Fig. 5), we found that Yoda1 treatment reduces OXPHOS in human ILC2s (Fig. 7 G), with basal respiration (Fig. 7 H), spare respiratory capacity (Fig. 7 I), and ATP production rates (Fig. 7 J) all reduced in hILC2s who were treated with Yoda1. In confirmation of our murine studies, we report that Piezo1 activation in human ILC2s is able to reduce ILC2 activation and oxidative metabolism.

Piezo1 activation reduces AHR and lung inflammation in humanized mice

To investigate the physiological role of Piezo1 activation in human ILC2 function, we next assessed whether Yoda1 could modulate the development of hILC2-dependent AHR and lung inflammation in humanized mice (Fig. S5, J and K) (Maazi et al., 2015). We therefore adoptively transferred pure populations of hILC2s into host $Rag2^{-/-}GC^{-/-}$ mice and measured the development of AHR and lung inflammation on day 4 in mice treated or not with Yoda1 intraperitoneally and i.n. with rhIL-33 for 3 consecutive days (Fig. 7 K). Compared with PBS-injected mice, we first found that control mice induced significantly more lung resistance (Fig. 7 L). In confirmation of our murine findings, however, Yoda1 treatment remarkably reduced the development of lung resistance in response to methacholine compared with vehicle controls (Fig. 7 L). Although identical numbers of ILC2s were initially transferred to both groups, we further found a net reduction in the number of hILC2s recovered in the lungs of Yoda1-treated mice compared with controls on day 4 (Fig. 7 M). Finally, and as expected, the numbers of eosinophils were lower in the BAL of Yoda1-treated mice compared to controls, indicating a reduced hILC2-driven lung inflammation following the activation of Piezo1 (Fig. 7 N). Importantly, Yoda1 administration in $Rag2^{-/-}GC^{-/-}$ mice without hILC2 adoptive transfer did not affect the development of AHR (Fig. S5, L and M). Taken together, our results reveal that Piezo1 is expressed on human ILC2s and that its activation with Yoda1 is able to reduce human ILC2-driven airway inflammation and AHR.

Discussion

Our major finding is that activation of Piezo1 channels in ILC2s ameliorates the development of AHR and lung inflammation in murine models and humanized mice. Using genetic deletion, we found that Piezo1 controls the magnitude of ILC2 function, as Piezo1 activation using Yoda1 reduces ILC2 function and development of AHR. Specifically, Piezo1 restrains ILC2s, as we found that hILC2-driven lung inflammation is reduced in humanized mice treated with Yoda1. To our knowledge, this is the first report identifying a role for Piezo1 channels in ILC2s, particularly in the lungs.

We screened the expression of all known MSCs in both naïve and activated lung ILC2s and showed compelling evidence that

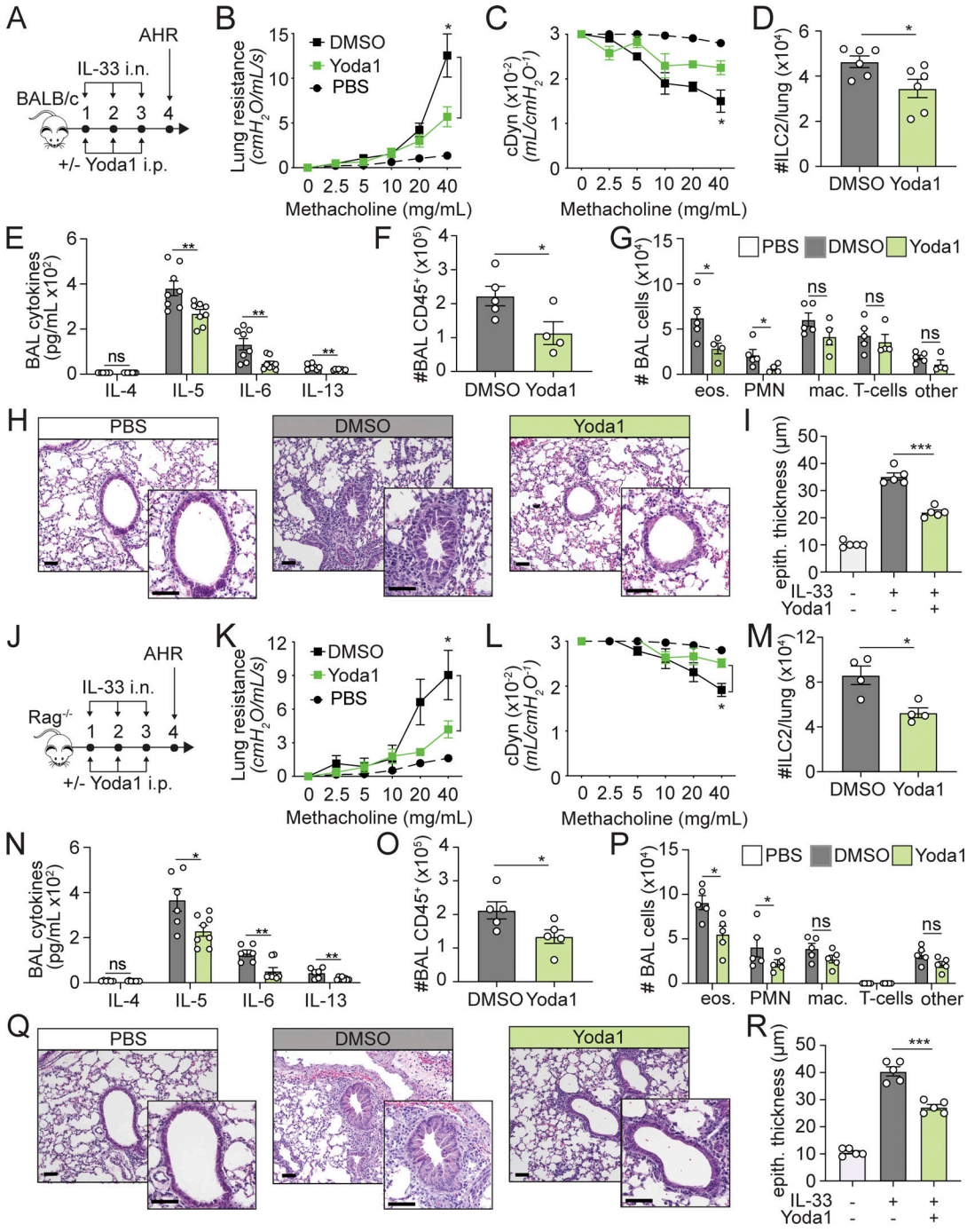

Figure 6. **In vivo Yoda1 treatment reduces AHR and lung inflammation. (A)** Schematic description of in vivo effects of Piezo1 activation on the development of AHR. BALB/c mice received intraperitoneal injections of 213 µg/kg/day Yoda1 or vehicle control and 0.5 µg rmIL-33 or PBS i.n. on days 1–3. On day 4, lung function, lung ILC2s, BAL cellularity, and histology were analyzed. **(B and C)** Lung resistance (B) and dynamic compliance (C) in response to increasing doses of methacholine. *n* = 5. The experiment was performed twice. **(D)** Total number of ILC2s per lung. *n* = 6. The experiment was performed twice. **(E)** Levels of IL-4, IL-5, IL-6, and IL-13 in the BAL. *n* = 8. The experiment was performed twice. **(F)** Total number of CD45⁺ lymphoid cells in the BAL. *n* = 5. The experiment was performed twice. **(G)** Numbers of BAL eosinophils (CD45⁺, CD11c⁻, SiglecF⁺), neutrophils (PMN, CD45⁺, SiglecF⁻, Ly6G⁺, CD11b⁺), macrophages (CD45⁺, Ly6G⁻, SiglecF⁻, CD11c⁺), T cells (CD45⁺, CD3⁺) and others. *n* = 5. The experiment was performed twice. **(H)** Lung histology. Scale bars, 50 µm. The experiment was performed twice. **(I)** Average alveolar epithelial thickness. *n* = 5. **(J)** Schematic description of in vivo effects of Piezo1 activation on the development of AHR. *Rag2*$^{-/-}$ mice received intraperitoneal injections of 213 µg/kg/day Yoda1 or vehicle control and 0.5 µg rmIL-33 or PBS i.n. on days 1–3. On day 4, lung function, lung ILC2s, BAL cellularity, and histology were analyzed. **(K and L)** Lung resistance (K) and dynamic compliance (L) in response to increasing doses of methacholine. *n* = 5. The experiment was performed three times. **(M)** Total number of ILC2s per lung. *n* = 4. The experiment was performed three times. **(N)** Levels of IL-4, IL-5, IL-6, and IL-13 in the BAL. *n* = 6. The experiment was performed three times. **(O)** Total number of CD45⁺ lymphoid cells in the BAL. *n* = 5. The experiment was performed three times. **(P)** Numbers of BAL eosinophils (CD45⁺, CD11c⁻, SiglecF⁺), neutrophils (PMN, CD45⁺, SiglecF⁻, Ly6G⁺, CD11b⁺), macrophages (CD45⁺, Ly6G⁻, SiglecF⁻, CD11c⁺), T cells (CD45⁺, CD3⁺), and others. *n* = 5. The experiment was performed three times. **(Q)** Lung histology. Scale

bars, 50 µm. The experiment was performed three times. **(R)** Average alveolar epithelial thickness. $n = 5$. Data are presented as mean ± SEM. A two-tailed Student's t test for unpaired data was applied for comparisons between two groups (D–G and M–P), except for multi-group comparisons where Tukey's multiple comparison one-way ANOVA tests were used (B, C, I, K, L, and R). *P < 0.05, **P < 0.01, ***P < 0.001.

Piezo1 is the most induced channel in response to activation. While we cannot rely solely on transcriptomic analysis, the use of transgenic mice expressing fluorescence under the Piezo1 promoter allowed us to confirm the expression of Piezo1 at the protein level. These mice are an important tool, as they have been previously used to measure the expression of Piezo1 on immune cells including regulatory T cells (Tregs) (Jairaman et al., 2021). Importantly, although adding Yoda1 to WT ILC2s significantly affected ILC2 function, it did not modulate ILC2s isolated from *Il7r*^{cre}*Piezo1*$^{fl/fl}$ mice. Whereas these findings validate the use of *Il7r*^{cre}*Piezo1*$^{fl/fl}$ mice as a genetic tool to assess the role of Piezo1 in ILC2s, they also importantly suggest that Piezo1 channels expressed on ILC2s are functionally active. We were however surprised with the dynamics of Piezo1 expression observed in our ex vivo studies. Although basal low levels are expressed at steady state, 24 h of activation was not sufficient to modulate the expression of Piezo1—a time point where multiple activation markers were previously reported on ILC2s (Hurrell et al., 2019; Lei et al., 2018). Piezo1 was nevertheless expressed both ex vivo and in vivo after 72 h of IL-33 stimulation. Further studies would be warranted to explain these observations, although they may highlight the unique role of Piezo1 in regulating ILC2 function.

We examined the role of Piezo1 in ILC2-driven lung inflammation by opposing two approaches: Piezo1 genetic deletion and Piezo1 pharmacological activation. Similar genetic approaches were previously used to monitor the role of Piezo1 in macrophages (Atcha et al., 2021) and T cells (Jairaman et al., 2021), whereas Yoda1 is widely considered a potent Piezo1 activator that induces Piezo1-specific calcium influx in multiple cells (Syeda et al., 2015). Overall, our findings are consistent with the involvement of Piezo1 in ILC2 function. Our transcriptomic analysis revealed that ILC2s lacking Piezo1 showed an overall upregulation of proinflammatory gene signatures, an observation we confirmed with the analysis of a previously published single-cell dataset (Wallrapp et al., 2017). We found elevated secretions of signature cytokines including IL-5 and IL-13, whereas ILC2 proliferation was significantly upregulated in the absence of Piezo1. As a result, the development of ILC2-dependent AHR was exacerbated. In sharp contrast, Yoda1 treatment inhibited ILC2 function, thus alleviating the symptoms associated with ILC2-dependent AHR and lung inflammation. Together, these two approaches therefore provide strong evidence that Piezo1 controls ILC2 function. Similarly, recent studies have shown that Piezo1 controls the function of immune cells including macrophages (Atcha et al., 2021), Tregs (Jairaman et al., 2021), or monocytes (Solis et al., 2019). Interestingly, however, the role of Piezo1 varies depending on the inflammatory context. For instance in macrophages, a study reports that Piezo1 activity promotes interferon-induced macrophage inflammation, although it suppresses IL-4/13–induced polarization by notably inhibiting inducible nitric oxide synthase expression and induces that of arginase (Atcha et al., 2021). Furthermore, a recent report shows that pharmacological inhibition of Piezo1 in ILC3s downregulates the expression of proinflammatory mediators and modulates intestinal immunity (Liu et al., 2023b). We, therefore, provide strong evidence that Piezo1 restrains type 2 inflammation in ILC2s, and whether these effects are specific to ILC2s or to type 2 inflammation, in general, remains to be elucidated.

Although the expression of Piezo1 in *Il7r*^{cre}*Piezo1*$^{fl/fl}$ mice was not significantly affected in other lung immune populations than ILC2s, the experiments describing the adoptive transfer of ILC2s lacking Piezo1 to alymphoid mice are essential to support our conclusions. Our results show that ILC2s lacking Piezo1 induce significantly more lung inflammation and AHR compared with controls, suggesting that Piezo1 channels control ILC2-driven inflammation independently of other immune cells. Regardless, we found that although ILC2s are the dominant population of ILCs following IL-33 challenge (Wallrapp et al., 2017), they still expressed significantly more Piezo1 compared with both ILC1 and ILC3. Similarly, they expressed more Piezo1 compared with T cells and myeloid populations, suggesting that ILC2s not only express and induce Piezo1 in the activated lungs but are also the dominant immune population to express it in our experimental setting.

Recently, we have shown that Orai1 and Orai2 ion channels modulate ILC2 metabolism and control the development of AHR and lung inflammation (Howard et al., 2023). Of note and in contrast to Piezo1, Orai1, and in particular Orai2, were expressed at steady state on ILC2s. Interestingly, a recent study deleted Piezo1 expression in CD4 cells and monitored the development of experimental autoimmune encephalomyelitis (EAE) (Jairaman et al., 2021). Deletion of Piezo1 did not affect T cell proliferation nor homing but significantly induced Treg expansion, thus reducing EAE severity. In particular, Piezo1 deletion enhanced transforming growth factor β (TGFβ) signaling. Similar to ILC2s, this study therefore suggests that Piezo1 controls the magnitude of Treg expansion and function in disease. Interestingly however, while this study showed that the absence of Piezo1 signaling in T cells was protective against EAE, another report showed that a gain of function mutation in T cells protected partially against malaria (Ma et al., 2018). These studies highlight the complex role of Piezo1 in immune cells as new roles for Piezo1 are emerging. For instance, Piezo1 serves as a central regulator of iron—a key nutritional trace element required by all cells—in mice and humans (Ma et al., 2021). Furthermore, Piezo1 can promote glycolysis in macrophages, therefore directly affecting the metabolism of immune cells (Leng et al., 2022). Whether Piezo1 affects different mechanisms in immune cells remains to be elucidated, as these studies highlight that Piezo1 regulation may have unique consequences on a cell, tissue or disease depending on the context.

The activation of MSCs induces downstream pathways that include the expression of MSTFs. Members of the Kruppel-like

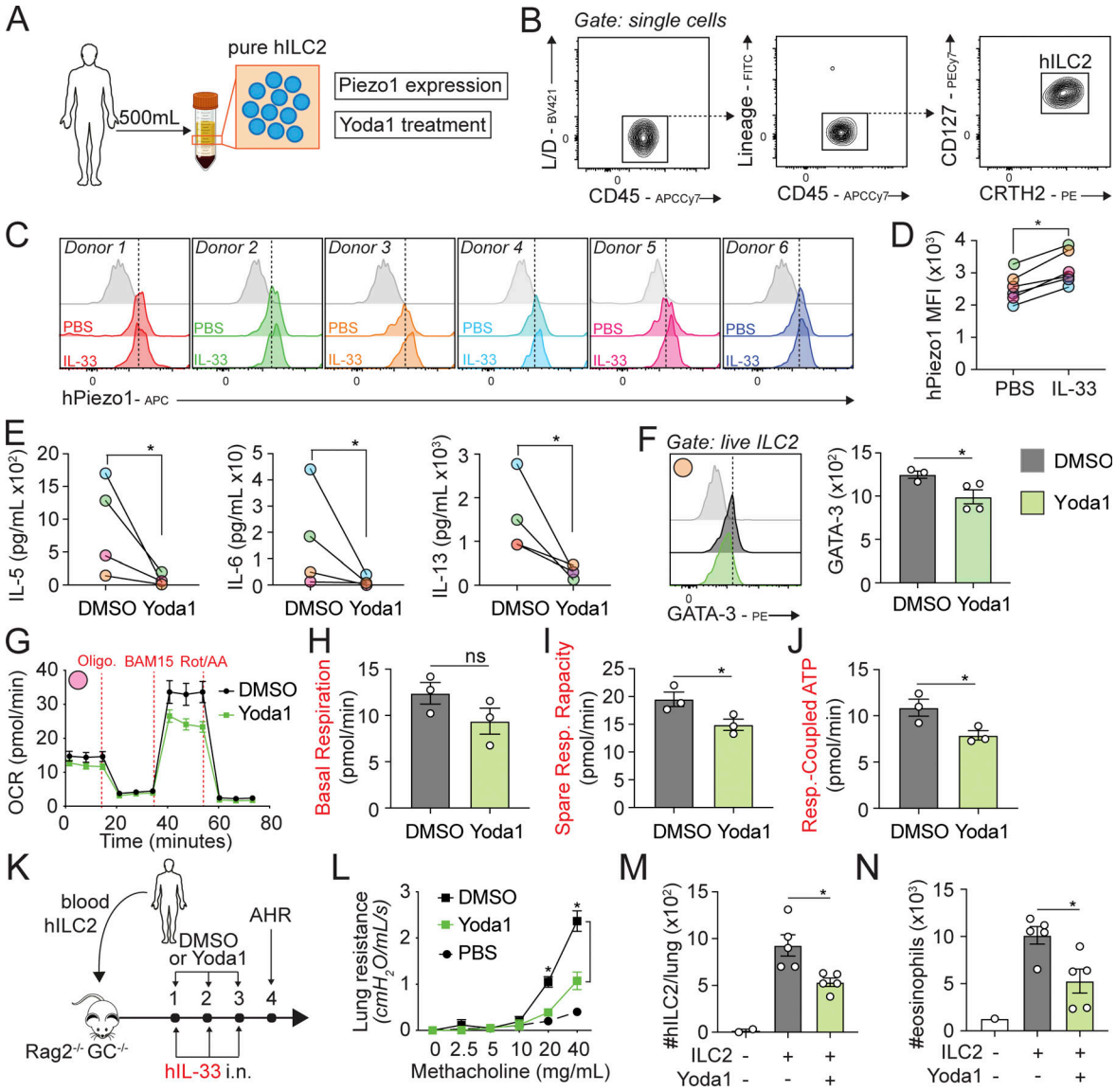

Figure 7. **Piezo1 controls human ILC2 function and development of AHR in humanized mice. (A)** Schematic description of human blood ILC2 isolation and experimental design. PBMCs were isolated from 500 ml of blood of six healthy subjects. After isolation of CD45⁺ Lineage⁻ CRTH2⁺ CD127⁺ hILC2s, cells were cultured (2 × 10^4/ml) in rhIL-2, rhIL-7 (both 20 ng/ml) with or without rhIL-33 (100 ng/ml) for 72 h. **(B)** Representative plots of hILC2 isolation purity. The experiment was performed six times. **(C and D)** Representative plots of Piezo1 expression from the six subjects (C) and corresponding quantitation presented as MFI (D). Gray histograms represent FMO: full-minus-one staining control. *n* = 6. **(E)** Levels of IL-5, IL-6, and IL-13 in the culture supernatants following treatment with 10 µM Yoda1. *n* = 4. **(F)** Representative plots of intranuclear GATA-3 expression and corresponding quantitation presented as MFI. *n* = 4. The experiment was performed three times. **(G–J)** Mitochondrial respiratory profile showing OCRs in response to oligomycin (ATP synthase inhibitor), BAM15 (mitochondrial uncoupler), and rotenone + antimycin A (complex I and II inhibitors) sequential injections (G) and corresponding key parameters of mitochondrial function (H) basal respiration, (I) spare respiratory, and (J) respiratory-coupled ATP. *n* = 3. The experiment was performed twice. **(K)** Schematic representation of the induction of airway inflammation by adoptively transferred human donor ILC2s in alymphoid recipients. PBMCs were isolated from 500 ml of blood from healthy subjects. After isolation of CD45⁺ Lineage⁻ CRTH2⁺ CD127⁺ hILC2s, cells were cultured (5 × 10^5/ml) in rhIL-2, rhIL-7 (both 20 ng/ml), and decreasing doses of rhIL-33 (100 ng/ml, 50 ng/ml, 25 ng/ml and 10 ng/ml) every 72 h or until the required number of cells was achieved. 1 × 10^5 human donor ILC2s were then subsequently transferred intravenously to *Rag2*$^{-/-}$*GC*$^{-/-}$ recipient mice, who then received 0.5 µg rmIL-33 i.n. on days 1–3. On day 4, lung function, lung ILC2s, and BAL cellularity were analyzed. The experiment was performed twice. **(L)** Lung resistance in response to increasing doses of methacholine. *n* = 3. **(M)** Total number of human ILC2s per lung. *n* = 5. **(N)** Total number of BAL eosinophils (CD45⁺, CD11c⁻, SiglecF⁺). *n* = 5. Data are presented as mean ± SEM and were performed with a total of eight donors. A two-tailed Student's *t* test for paired data was applied for comparisons between two groups (D and E). A two-tailed Student's *t* test for unpaired data was applied for comparisons between two groups (F and H–J), except for multigroup comparisons where Tukey's multiple comparison one-way ANOVA tests were used (L–N). *P < 0.05 and ns: non-significant.

transcription factors family—including in particular KLF2—are MSTFs that control the function of immune cells including monocytes, macrophages and T cells (Turpaev, 2020). Importantly, although KLF2 controls the expression of multiple genes, KLF2-mediated inhibition of NF-κB signaling leads to the suppression of pro-inflammatory cytokines (Jha and Das, 2017). Our results show that Piezo1 activation induces KLF2 expression associated with a decrease in NF-κB signaling. In direct support to our findings, Piezo1 activation using Yoda1 in endothelial cells rapidly induced KLF2 signaling (Zheng et al., 2022). In addition, the authors found that KLF2 was able to restrain the TNF-induced NF-κB activation and promote anti-inflammatory effects. In line with these findings, our results provide evidence that induction of KLF2 in ILC2s is linked to a decrease in pro-inflammatory signature. Experiments using KLF2 inducer SAHA confirmed this observation. Nevertheless, vorinostat (SAHA) is a histone deacetylase inhibitor used to treat patients against several diseases, and although it potently induces KLF2, other downstream mechanisms may differently affect cellular activation. Interestingly however, several drugs with the ability to induce KLF2—including SAHA—have emerged as potential novel therapies in the context of atherosclerosis (Dabravolski et al., 2022). Our findings therefore identify KLF2 signaling as a downstream mechanism of Piezo1 signaling in ILC2s.

We and others have previously shown that ILC2s heavily rely on mitochondrial activity (Wilhelm et al., 2016; Galle-Treger et al., 2020). In the present study, our results suggest that Piezo1 controls ILC2 oxidative energy as Piezo1 activation reduces oxidative respiration and ILC2 function. In support of our findings, a recent study reported a role for Piezo1 on macrophage metabolism (Leng et al., 2022). In particular, Piezo1 deletion in macrophages showed a tendency toward increased OXPHOS associated with reduced aerobic glycolysis, as Yoda1 treatment significantly upregulated glycolytic activity. Furthermore, Piezo1 activation also potentially induced a glycolytic phenotype in DCs (Chakraborty et al., 2021). Interestingly, our analysis revealed the upregulation of glycolytic genes in combination with reduced TCA cycle activity and fatty acid metabolism gene signatures, suggesting that similar to the role of Piezo1 in macrophage metabolism, Piezo1 may control ILC2 metabolic activities. Mechanistically, the inhibitory effects of Yoda1 on ILC2 oxidative metabolism were reproduced using KLF2 inducer SAHA, suggesting that KLF2—previously shown to drive endothelial cell metabolism (Doddaballapur et al., 2015)—is involved in the process. In line with these findings, the decrease in NF-κB p65 observed following both Yoda1 and SAHA treatments may likely contribute to the decrease in OXPHOS in ILC2s, as NF-κB was shown to regulate the expression of TCA core enzymes (Zhou et al., 2017). In particular, NF-κB controls the expression of IDH1, IDH3A, and ACO2, which were all reduced by Yoda1 in our transcriptomic analysis.

Our results suggest that Piezo1 activation in ILC2s might be exclusive to inflammatory conditions, with IL-33 being the most potent cytokine to induce Piezo1. Notably, however, IL-25 induced Piezo1 on ILC2s, albeit at a lower magnitude compared with IL-33, whereas TSLP showed a relatively minor but statistically significant induction of Piezo1 compared with controls. Since IL-33 is more potent than IL-25 and TSLP to activate ILC2s (Barlow et al., 2013; Camelo et al., 2017), these findings suggest that the magnitude of Piezo1 expression may therefore directly be linked to the level of ILC2 activation. We confirmed this hypothesis using neuropeptides, known to modulate the ILC2 function (Wallrapp et al., 2017; Pascal et al., 2022). In confirmation of our protein analysis, IL-33 induced significantly more Piezo1 compared with IL-25. However, although Neuromedin U (NMU) alone induced modest levels of Piezo1, the combination of NMU and IL-25 potently induced Piezo1 expression to levels close to those observed after the IL-33 challenge. Since NMU was shown by the authors to upregulate the expression of IL-25R (Wallrapp et al., 2017), these findings therefore support the notion that the magnitude of Piezo1 may directly be linked to the level of ILC2 activation. It is important to note that we also confirmed the induction of Piezo1 by physiologically relevant allergens. Upon *A. alternata* exposure, its serine protease activity causes rapid IL-33 release in the lungs (Snelgrove et al., 2014), as we observed an induction of Piezo1 following the administration of the allergen in vivo. Despite the complexity of the IL-33 receptor signaling cascade (Pinto et al., 2018), our study indicates a link between IL-33 and Piezo1 induction. It may, however, result not only from multiple crossreacting signaling cascades, including NF-κB, but also several MAP kinases, AKT, JAK/STAT, cJUN, or CREB1. Furthermore, since Piezo1 activation itself indirectly affects NF-κB p65 production in ILC2s, the identification of the pathways inducing Piezo1 downstream of the IL-33 receptor may prove to be even more challenging.

So far, mechanical stimuli remain the exclusive activators of Piezo1. However, human and mouse Piezo1 are selectively activated by micromolar concentrations of the small molecule Yoda1 (Syeda et al., 2015). Multiple factors in vivo induce mechanical force in a cell during activation, including ligand–receptor interactions, which lead to dynamic cytoskeletal remodeling and shape change, inducing shear stress on the cell membrane (Kumari et al., 2014). It is now clear that mechanical force in activated cells is generated by myosin-II–based pulling and the generation of actin polymerization such as the Arp2/3 nucleation complex (Vicente-Manzanares et al., 2009; Matsumura, 2005; Chesarone et al., 2010). Interestingly, a quantitative phosphoproteomic analysis revealed that IL-33 activates the cdc42/Rho signaling pathway, essential for actin cytoskeleton reorganization (Pinto et al., 2015). We notably confirm the upregulation of actin remodeling pathways in murine lung ILC2s by IL-33 (Fig. S1 E). Previous investigations, coupled with our analysis, therefore suggest that ILC2 activation by the IL-33/IL-33 receptor axis may naturally contribute to the production of mechanical stress on the membrane of ILC2s.

We confirmed the observations from our murine studies using human ILC2s isolated from the PBMCs of healthy donors. Importantly, Piezo1 was expressed and induced by human ILC2s in the presence of rhIL-33 as Yoda1 treatment reduced ILC2 activation, as evidenced by reduced inflammatory cytokines secretion. Furthermore, we confirmed that Piezo1 activation reduced human ILC2 oxidative metabolism in our bioenergetic assays. While these findings support that Piezo1 activation reduces human ILC2 function, we further confirmed the role of

Piezo1 in modulating the induction of AHR in humanized mice (Maazi et al., 2015). Remarkably, the treatment of humanized mice with Yoda1 reduced AHR and lung inflammation, therefore suggesting that Yoda1 may be used as a therapeutic tool to modulate ILC2 function and alleviate the symptoms associated with ILC2-dependent airway inflammation in humans. Future studies are therefore warranted to delineate the expression patterns and function of Piezo1 channels in human patients with asthma. In particular, identifying Piezo1-expressing ILC2s and their relation to disease severity may provide valuable information for the development of Piezo1-driven therapeutics for the treatment of allergic asthma pathogenesis in human patients.

Collectively, our studies identified the role of Piezo1 channels in ILC2-driven AHR and lung inflammation. Our main findings suggest that Piezo1 activation reduced ILC2 function and metabolism, in turn reducing the induction of AHR in murine and humanized mice models. Given the importance of ILC2s in allergic asthma and the need for novel mechanism-based approaches to target the main drivers of inflammation in particular in the lungs, we propose that Piezo1 activation could represent a novel mechanism-based approach for the treatment of ILC2-driven allergic asthma.

Materials and methods

Animal studies

5- to 8-wk-old sex-matched mice were used in all experiments. WT BALB/cByJ (RRID:IMSR_JAX:001026), *Rag2*$^{-/-}$ (C.B6(Cg)-Rag2$^{tm1.1Cgn}$/J, RRID:IMSR_JAX:008448), *Rag2*$^{-/-}$ *IL-2Rg*$^{-/-}$ (*Rag2*$^{-/-}$*GC*$^{-/-}$, C;129S4-Rag2tm1.1FlvIl2rgtm1.1Flv/J, RRID:IMSR_JAX:014593), Piezo1dT (B6;129-*Piezo1*$^{tm1.1Apat}$/J, RRID:IMSR_JAX:029214), and *Piezo1*$^{fl/fl}$ (B6.Cg-*Piezo1*$^{tm2.1Apat}$/J, RRID:IMSR_JAX:029213) mice were all purchased from the Jackson Laboratories. All mice were on a BALB/c background except Piezo1dT and *Piezo1*$^{fl/fl}$, who were on a C57BL/6 background. *Il7*^{cre}*Piezo1*$^{fl/fl}$ mice on a C57BL/6 background were generated by breeding *Il7*^{cre} (a gift from Dr. Homayon Ghiasi, Cedars-Sinai, Los Angeles, CA, USA) and *Piezo1*$^{fl/fl}$ together. *Il7*$^{cre/+}$*Piezo1*$^{fl/fl}$ mice were used in experiments, and *Il7*$^{cre/+}$ littermates were used as controls. All mice were maintained and bred in a pathogen-free animal facility at the Keck School of Medicine, University of Southern California (USC) under protocols approved by the Institutional Animal Care and Use Committee.

Human studies

Effects of Piezo1 channels on human ILC2 function and the development of AHR in humanized mice was investigated. Peripheral blood samples of eight healthy anonymous adult volunteers were obtained following written consent. All participants were clinically well. Experimental protocols were approved by the USC Institutional Review Board and conducted in accordance with the principles of the Declaration of Helsinki.

In vivo murine experiments and tissue preparation

Mice were challenged i.n. on 3 consecutive days with rmIL-33 (0.5 µg in 50 µl PBS; BioLegend) or PBS under anesthesia. For *A. alternata* experiments, mice were challenged on 4 consecutive days i.n. with 100 µg/mouse of *A. alternata* (Greer Laboratories) under anesthesia. In some experiments, mice were also challenged i.n. on 3 consecutive days with rmIL-25 (0.5 µg in 50 µl PBS; BioLegend) or rmTSLP (0.5 µg in 50 µl PBS; R&D Systems). When indicated, Yoda1 (213 µg/kg; Tocris Bioscience) or SAHA (100 mg/kg; Sigma-Aldrich) were intraperitoneally administered in 200 µl PBS prior to each intranasal challenge. For murine adoptive transfer experiments, 50 × 10^3 pure ILC2s were injected via the tail vein in a total volume of 200 µl sterile PBS 1× to *Rag2*$^{-/-}$ *IL-2Rg*$^{-/-}$ alymphoid hosts. Recipients were further challenged i.n. on days 1–3 with rmIL-33. 24 h following the last intranasal, lungs were collected, processed to single-cell suspension, and analyzed for the indicated readouts. Briefly, following transcardial perfusion with PBS 1×, collected lungs were digested in collagenase Type IV (400 U/ml; Worthington) diluted in PBS at 37°C for 1 h on a shaker (200 rpm) and processed to single cell suspension through a 70-µm nylon cell strainer (Falcon). Lung cell suspensions were further treated with red blood cell (RBC) lysis buffer (BioLegend) and used for the indicated readouts.

Flow cytometry

The following murine antibodies were used: FITC anti-mouse lineage (CD3ε [145-2C11, RRID: AB_312670], CD4 [GK1.5, RRID: AB_312690], CD5 [53-7.3, RRID: AB_312734], TCRβ [H57-597, RRID: AB_313428], TCRγδ [UC7-13D5, RRID: AB_313312], B220/CD45R [RA3-6B2, RRID: AB_312990], Gr-1 [RB6-8C5, RRID: AB_313370], CD11c [N418, RRID: AB_313774], CD11b [M1/70, RRID: AB_312788], Ter119 [TER-119, RRID: AB_313706], FcεRIa [MAR-1, RRID: AB_1626102], CD335 [29A1.4, RRID: AB_2149150]), PE-Cy7 anti-mouse CD127 (A7R34, RRID: AB_1937266), APCCy7 anti-mouse CD45 (30-F11, RRID: AB_312980), PECy7 anti-mouse CD45 (30-F11, RRID: AB_312978), BV650 anti-mouse CD45 (30-F11, RRID: AB_2565884), APCCy7 anti-mouse CD11c (N418, AB_830646), FITC anti-mouse CD19 (6D5, RRID: AB_313640), APC anti-mouse SiglecF (S17007L, RRID: AB_2750236), APC anti-mouse Ly6G (1A8, RRID: AB_1877163), BV785 anti-mouse Ly6G (1A8, AB_2566317), APCCy7 anti-mouse Ly6C (HK1.4, RRID: AB_10643867), BV711 anti-mouse Ly6C (HK1.4, RRID: AB_2562630), and PerCPCy5.5 anti-mouse CD3ε (17A2, RRID: AB_1595597) were purchased from BioLegend. PE anti-mouse SiglecF (E50-2440, RRID: AB_394341) was purchased from BD Biosciences. PerCP-eFluor710 anti-mouse ST2 (RMST2-2, AB_2573883) and eFluor450 anti-mouse CD11b (M1/70, AB_1582236) were purchased from Thermo Fisher Scientific. Intranuclear staining was performed using the Foxp3 Transcription Factor Staining Kit (Thermo Fisher Scientific) according to the manufacturer's instructions and APC anti-mouse Ki67 (SolA15, RRID: AB_2688057; Thermo Fisher Scientific), PE anti-mouse/human GATA-3 (TWAJ; Thermo Fisher Scientific), eFluor 450 anti-mouse/human GATA-3 (TWAJ, RRID: AB_1963600; Thermo Fisher Scientific), APC anti-mouse T-bet (4B10, RRID: AB_2744712; Thermo Fisher Scientific), PerCP-eFluor 710 anti-mouse ROR gamma (t) (B2D, RRID: AB_10717956; Thermo Fisher Scientific), PE anti-mouse/human RelA/NF-κB p65 (532301; R&D), and AF647 anti-mouse/human polyclonal KLF2 (1:500; Thermo Fisher Scientific) were used. Intracellular staining was performed using the BD Cytofix/Cytoperm kit (RRID: AB_2869008) and used

according to the manufacturer's instructions. Cells were stimulated 4 h ex vivo with 50 µg/ml PMA, 500 µg/ml ionomycin (both Sigma-Aldrich), and 1 µg/ml Golgi plug (BD Biosciences), and PE anti-mouse IL-13 (eBio13A, RRID: AB_763559; Thermo Fisher Scientific) and APC anti-mouse/human IL-5 (TRFK5, RRID: AB_315329; BioLegend) were used. For apoptosis staining, PE Annexin V (Thermo Fisher Scientific) and DAPI (Sigma-Aldrich) were used according to the manufacturer's instructions. All antibodies were used at 1:200 unless stated differently.

The following human antibodies were used: FITC anti-human lineage cocktail (RRID: AB_10612570) including CD3 (clone UCHT1), CD14 (clone HCD14), CD16 (clone 3G8), CD19 (clone HIB19), CD20 (clone 2H7), CD56 (clone HCD56). The following additional lineage markers were added: FITC anti-human CD235a (Clone HI264, RRID: AB_10612923), FITC anti-human FCεRIa (clone AER-37, RRID: AB_1227654), FITC anti-human CD1a (clone HI149, RRID: AB_314017), FITC anti-human CD123 (clone 6H6, RRID: AB_755989) and FITC anti-human CD5 (clone L17F12). APCCy7 anti-human CD45 (HI30, RRID: AB_314402), PECy7 anti-human CD127 (A019D5, RRID: AB_3068286) and PE anti-human CRTH2 (BM16, RRID: AB_10900255), all purchased from BioLegend. For Piezo1 staining, ILC2s were first stained on ice with rabbit anti-mouse/human Piezo1 (15939-AP, Proteintech, 1:100, RRID: AB_2231460) and then with Alexa Fluor 647 goat anti-rabbit (H+L) (1:200, RRID: AB_2535812; Thermo Fisher Scientific), both for 1 h (Caulier et al., 2020). Live/dead fixable violet or aqua cell stain kits were used to exclude dead cells (Thermo Fisher Scientific) and CountBright absolute counting beads were used (Thermo Fisher Scientific) to calculate absolute cell numbers when indicated. Stained cells were analyzed on a FACSCanto II system, and data were analyzed with FlowJo version 10 software.

Murine ILC2 isolation and ex vivo culture

ILC2s were FACS-sorted to a purity of >95% on a FACSARIA III system from the lungs of mice challenged on 3 consecutive days i.n. with rmIL-33. ILC2s were gated as live lineage (CD3e, CD4, CD5, TCRb, TCRgd, CD45R/B220, CD335, CD11c, CD11b, Gr1, FceRIa, and Ter119) negative $CD45^+$, $ST2^+$, and $CD127^+$ cells. In studies focusing on $Piezo1^{low}$ and $Piezo1^{high}$ ILC2s, ILC2s were further sorted based on their expression of Piezo1dT (20% low and 20% high). Isolated ILC2s were washed in PBS 1× and cultured ex vivo for the indicated times at 37°C (5×10^4/ml) in 96-well U-bottom plates with rmIL-2 (10 ng/ml; BioLegend) and rmIL-7 (10 ng/ml; BioLegend) in complete RPMi (cRPMi) supplemented with 10% heat-inactivated FBS (Omega Scientific), 100 U/ml penicillin, and 100 mg/ml streptomycin (GenClone). For immunoblotting, 1.5×10^6/ml ILC2s were plated in 24-cell plates. In studies focusing on the role of Piezo1 channel engagement, 10 µM Yoda1 or 1 µM SAHA (Sigma-Aldrich) with corresponding DMSO control were further added to cultures for the indicated times. When indicated, NMU-23 (100 ng/ml; Phoenix Pharmaceuticals) and VIP (10 µM; Tocris) or vehicle controls were used.

Immunoblotting

After culture, ILC2s were lysed in radioimmunoprecipitation assay lysis buffer (EMD Millipore) supplemented with protease inhibitor cocktail (Roche) for 30 min. Lysates were centrifuged (13,000 *g* at 4°C for 15 min) and the supernatants were collected. Protein concentrations were determined using the Pierce BCA Protein Assay Kit (Thermo Fisher Scientific) and samples were adjusted to the same concentration. The adjusted protein eluates were mixed with 6× Laemmli SDS sample buffer (Bioland Scientific) and heated at 95°C for 5 min. Protein eluates were resolved by SDS-PAGE and transferred to a poly(vinylidene fluoride) membrane (Bio-Rad). Membranes were blocked with 5% BSA and probed with rabbit anti-KLF2 (1:500; Sigma-Aldrich Millipore) and rabbit anti-HSP90 (1:2,000; Proteintech) at 4°C overnight. Membranes were incubated with horseradish peroxidase (HRP)–conjugated goat secondary antibodies (1:1,000; Invitrogen). Immunodetection was achieved by ProSignal Pico Spray (Genesee Scientific) and detected on a ChemiDoc Imaging System (Bio-Rad).

Bioenergetic assays

The real-time OCR was measured using a Seahorse Mini HS XF instrument (Agilent). Following the indicated experimental design, 3×10^4 FACS-sorted ILC2s were plated on a Seahorse XFp PDL-coated cell culture miniplate in triplicates in FBS/Phenol red free Seahorse media supplemented with 1 mM pyruvate, 2 mM glutamine, and 10 mM glucose. A T cell metabolic profiling assay was then performed (Agilent). Briefly following baseline measurements, 1.5 µM oligomycin, 2.5 µM BAM15, and 0.5 µM rotenone/antimycin A were sequentially injected in the culture, and oxygen levels were measured in triplicates following each injection.

Measure of lung function and BAL collection

Measurements of airway resistance were conducted using the FinePointe RC system (Buxco Research Systems) in which anesthetized mice were mechanically ventilated. Mice were sequentially challenged with aerosolized PBS (baseline) followed by increasing doses of methacholine (Sigma-Aldrich) ranging from 2.5 to 40 mg/ml. Maximum resistance was recorded during a 3-min period following each challenge as we continuously computed lung resistance (R_L) by fitting flow, volume, and pressure to an equation of motion. When indicated, BAL fluid was collected. Briefly, the lungs were washed three times with 1 ml ice-cold PBS 1× to collect cells. BAL supernatants were stored for cytokine measurement assays, and BAL cell suspensions were further treated with RBC lysis buffer prior to use for flow cytometry analysis of inflammatory cells.

Histology

Lungs were collected and stored in paraformaldehyde 10%. Tissues were then embedded in paraffin, and sections of 4 mm were prepared for hematoxylin and eosin (H&E) staining. Histology pictures were acquired on a KeyenceBZ-9000 microscope (Keyence) and assembled into multipaneled figures using Adobe Illustrator software (version 22.1). Epithelial thickness was analyzed with the ImageJ analysis software (National Institutes of Health).

RNA-seq and data analysis

Cultured ILC2s were recovered, lysed in RLT buffer (Qiagen), and RNA was extracted using the MicroRNeasy kit (Qiagen). For each sample, a total of 10 pg of RNA was used to generate cDNA

(SMARTer Ultra Low Input RNA v3 kit, Clontech) for library preparation. Samples were then amplified and sequenced on a NextSeq 500 system (Illumina), where on average 30 million reads were generated from each sample. Raw reads were then further processed on Partek Flow software, version 10.0 (Partek Inc). Briefly, raw reads were trimmed by quality score (min Phred score 20 from both ends and trimmed reads shorter than 25 bp were discarded). Trimmed reads were aligned by STAR—2.7.8.a with mouse reference index mm10 and GENECODE M25 annotations. Aligned reads were further quantified to Gencode M25 with Partek E/M algorithm. Genes with <10 counts in all samples were removed from the analysis. The remaining genes were subjected to differential expression analysis by DESeq2 with median ratio normalization. Comparative functional enrichment analysis was performed on QIAGEN IPA (QIAGEN, Inc., https://digitalinsights.qiagen.com/IPA). For the single-cell RNA-seq (scRNA-seq) analysis, raw files were downloaded and analyzed as previously described (Wallrapp et al., 2017). The initial quality control, preprocessing, and dimensionality reduction of scRNA-seq data were performed using the R programming language (version 4.3.0) and the Seurat package (version 4.9.9). The creation of graphical representations and data visualizations involved the utilization of several R packages, including the circlize package (version 0.4.15) for chord diagrams and the fmsb package (version 0.7.5) for radar plots. Additionally, the ggplot2 package (version 3.4.3) was employed for the customization of various plot elements and the generation of clear, data-driven visualizations. Raw and processed data for Fig. 2 (GSE255882) and Fig. 5 (GSE255881) were deposited in the Gene Expression Omnibus database.

Human ILC2 isolation, culture, and humanized mice

Human peripheral blood ILC2s were isolated from total PBMCs from a total of eight individual donors to a purity of >95% on a FACSARIA III system. Briefly, human fresh blood was first diluted 1:1 in PBS 1×, and PBMCs were isolated using SepMate-50 separation tubes (STEMCELL Technologies) and used according to the manufacturer's instructions. RBC lysis (BioLegend) was performed and CRTH2$^+$ cells were then isolated using the CRTH2 MicroBead Kit (Myltenyi Biotec), and used according to the manufacturer's instructions. Human ILC2s were identified as CD45$^+$, Lineage$^-$ (CD3, CD5, CD14, CD16, CD19, CD20, CD56, CD235a, CD1a, CD123), CD127$^+$, and CRTH2$^+$. Isolated ILC2s were cultured at 37°C (2 × 10^4/ml) for 72 h in cRPMi supplemented with rhIL-2 (20 ng/ml; BioLegend) and rhIL-7 (20 ng/ml; BioLegend) with or without rhIL-33 (100 ng/ml; BioLegend) in U-bottom 96-well plates. When indicated, 10 µM Yoda1 or corresponding DMSO control was added to cultures for the indicated readouts. For experiments involving humanized mice, isolated human ILC2s were cultured with rhIL-2, rhIL-7, and rhIL-33 for 3–7 days (culture medium was changed every 2–3 days) until the required number of ILC2s was achieved prior to the transfer of 1 × 10^5 ILC2s intravenously to *Rag2*$^{-/-}$*GC*$^{-/-}$ alymphoid hosts. Mice were then challenged on 3 consecutive days with 0.5 µg/mouse of carrier-free rhIL-33 (BioLegend) diluted in 50 µl PBS under anesthesia, and Yoda1 (Tocris Bioscience) was intraperitoneally administered (213 µg/kg) in 200 µl PBS prior each intranasal challenge.

Cytokine measurements

Culture and BAL supernatants were collected and cytokines were measured using the LEGENDplex Mouse Th2 Panel (BioLegend), and used according to the manufacturer's instructions. For human cytokine measurements, culture supernatants were collected and cytokines were measured using the LEGENDplex Human Th2 Panel (BioLegend).

Statistical analysis

Data are presented as mean + SEM and analyzed using GraphPad Prism software (version 9.5.1). A two-tailed Student's *t* test for unpaired or paired data was applied for comparisons between two groups, except for multigroup comparisons where Tukey's multiple comparisons one-way ANOVA tests were used.

Online supplemental material

Fig. S1 describes gating strategies used throughout the manuscript and shows additional data on the effects of apoptosis of cultured cells and a deeper analysis of single-cell transcriptomic data focusing on the effects of IL-33 on actin pathways in ILC2s. Fig. S2 focuses on the effects of other ILC2 activators on the expression of Piezo1 at both transcriptomic and protein levels, including IL-25, TSLP, VIP, and NMU. Fig. S3 characterizes *Il7r*^{cre}*Piezo1*$^{fl/fl}$ mice used in our manuscript. Fig. S4 provides additional data on the role of Yoda1 and SAHA on ILC2s at the transcriptomic and protein levels. Fig. S5 presents a comprehensive analysis of the in vivo Yoda1 challenge using *A. alternata*, as well as providing supportive data on the humanized mouse model used in Fig. 7.

Data availability

Data are available in the article itself and its online supplementary materials. Bulk RNA-seq data generated in this study have been deposited in the Gene Expression Omnibus and are publicly available: Fig. 2 (GSE255882) and Fig. 5 (GSE255881). This paper analyzes existing, publicly available scRNA-seq data (GSE102299).

Acknowledgments

This article was financially supported by National Institutes of Health Public Health Service grants R01 HL144790, R01 HL151493, R01 AI145813, and R01 HL159804 (O. Akbari). Graphical abstract was designed with Biorender.com.

Author contributions: Conceptualization: B.P. Hurrell and O. Akbari. Methodology: B.P. Hurrell, O. Akbari, Y. Sakano, S. Shen, P. Shafiei-Jahani, M.H. Kazemi, K. Sakano, X. Li, H. Ghiasi, and C. Quach. Funding acquisition: O. Akbari. Supplied material: H. Ghiasi. Human samples acquisition: B.P. Hurrell and P. Shafiei-Jahani. Supervision: O. Akbari. Writing—original draft: B.P. Hurrell, O. Akbari, S. Shen. Writing—review and editing: B.P. Hurrell, O. Akbari, Y. Sakano, S. Shen, P. Shafiei-Jahani, M.H. Kazemi, K. Sakano, X. Li, H. Ghiasi, and C. Quach. Supplied mice: H. Ghiasi.

Disclosures: The authors declare no competing interests exist.

Submitted: 9 October 2023
Revised: 16 January 2024
Accepted: 22 February 2024

References

Asaoka, M., H. Kabata, and K. Fukunaga. 2022. Heterogeneity of ILC2s in the lungs. *Front. Immunol.* 13:918458. https://doi.org/10.3389/fimmu.2022.918458

Atcha, H., A. Jairaman, J.R. Holt, V.S. Meli, R.R. Nagalla, P.K. Veerasubramanian, K.T. Brumm, H.E. Lim, S. Othy, M.D. Cahalan, et al. 2021. Mechanically activated ion channel Piezo1 modulates macrophage polarization and stiffness sensing. *Nat. Commun.* 12:3256. https://doi.org/10.1038/s41467-021-23482-5

Barlow, J.L., S. Peel, J. Fox, V. Panova, C.S. Hardman, A. Camelo, C. Bucks, X. Wu, C.M. Kane, D.R. Neill, et al. 2013. IL-33 is more potent than IL-25 in provoking IL-13-producing nuocytes (type 2 innate lymphoid cells) and airway contraction. *J. Allergy Clin. Immunol.* 132:933–941. https://doi.org/10.1016/j.jaci.2013.05.012

Cahalan, S.M., V. Lukacs, S.S. Ranade, S. Chien, M. Bandell, and A. Patapoutian. 2015. Piezo1 links mechanical forces to red blood cell volume. *Elife*. 4:e07370. https://doi.org/10.7554/eLife.07370

Camelo, A., G. Rosignoli, Y. Ohne, R.A. Stewart, C. Overed-Sayer, M.A. Sleeman, and R.D. May. 2017. IL-33, IL-25, and TSLP induce a distinct phenotypic and activation profile in human type 2 innate lymphoid cells. *Blood Adv.* 1:577–589. https://doi.org/10.1182/bloodadvances.2016002352

Caulier, A., N. Jankovsky, Y. Demont, H. Ouled-Haddou, J. Demagny, C. Guitton, L. Merlusca, D. Lebon, P. Vong, A. Aubry, et al. 2020. PIEZO1 activation delays erythroid differentiation of normal and hereditary xerocytosis-derived human progenitor cells. *Haematologica*. 105:610–622. https://doi.org/10.3324/haematol.2019.218503

Chakraborty, M., K. Chu, A. Shrestha, X.S. Revelo, X. Zhang, M.J. Gold, S. Khan, M. Lee, C. Huang, M. Akbari, et al. 2021. Mechanical stiffness controls dendritic cell metabolism and function. *Cell Rep.* 34:108609. https://doi.org/10.1016/j.celrep.2020.108609

Chesarone, M.A., A.G. DuPage, and B.L. Goode. 2010. Unleashing formins to remodel the actin and microtubule cytoskeletons. *Nat. Rev. Mol. Cell Biol.* 11:62–74. https://doi.org/10.1038/nrm2816

Coste, B., J. Mathur, M. Schmidt, T.J. Earley, S. Ranade, M.J. Petrus, A.E. Dubin, and A. Patapoutian. 2010. Piezo1 and Piezo2 are essential components of distinct mechanically activated cation channels. *Science*. 330:55–60. https://doi.org/10.1126/science.1193270

Dabravolski, S.A., V.N. Sukhorukov, V.A. Kalmykov, A.V. Grechko, N.K. Shakhpazyan, and A.N. Orekhov. 2022. The role of KLF2 in the regulation of atherosclerosis development and potential use of KLF2-targeted therapy. *Biomedicines*. 10:254. https://doi.org/10.3390/biomedicines10020254

Das, H., A. Kumar, Z. Lin, W.D. Patino, P.M. Hwang, M.W. Feinberg, P.K. Majumder, and M.K. Jain. 2006. Kruppel-like factor 2 (KLF2) regulates proinflammatory activation of monocytes. *Proc. Natl. Acad. Sci. USA*. 103:6653–6658. https://doi.org/10.1073/pnas.0508235103

Diem, K., M. Fauler, G. Fois, A. Hellmann, N. Winokurow, S. Schumacher, C. Kranz, and M. Frick. 2020. Mechanical stretch activates piezo1 in caveolae of alveolar type I cells to trigger ATP release and paracrine stimulation of surfactant secretion from alveolar type II cells. *FASEB J.* 34:12785–12804. https://doi.org/10.1096/fj.202000613RRR

Doddaballapur, A., K.M. Michalik, Y. Manavski, T. Lucas, R.H. Houtkooper, X. You, W. Chen, A.M. Zeiher, M. Potente, S. Dimmeler, and R.A. Boon. 2015. Laminar shear stress inhibits endothelial cell metabolism via KLF2-mediated repression of PFKFB3. *Arterioscler. Thromb. Vasc. Biol.* 35:137–145. https://doi.org/10.1161/ATVBAHA.114.304277

Friedrich, E.E., Z. Hong, S. Xiong, M. Zhong, A. Di, J. Rehman, Y.A. Komarova, and A.B. Malik. 2019. Endothelial cell Piezo1 mediates pressure-induced lung vascular hyperpermeability via disruption of adherens junctions. *Proc. Natl. Acad. Sci. USA*. 116:12980–12985. https://doi.org/10.1073/pnas.1902165116

Galle-Treger, L., B.P. Hurrell, G. Lewis, E. Howard, P.S. Jahani, H. Banie, B. Razani, P. Soroosh, and O. Akbari. 2020. Autophagy is critical for group 2 innate lymphoid cell metabolic homeostasis and effector function. *J. Allergy Clin. Immunol.* 145:502–517.e5. https://doi.org/10.1016/j.jaci.2019.10.035

Geng, J., Y. Shi, J. Zhang, B. Yang, P. Wang, W. Yuan, H. Zhao, J. Li, F. Qin, L. Hong, et al. 2021. TLR4 signalling via Piezo1 engages and enhances the macrophage mediated host response during bacterial infection. *Nat. Commun.* 12:3519. https://doi.org/10.1038/s41467-021-23683-y

Halim, T.Y.F., B.M.J. Rana, J.A. Walker, B. Kerscher, M.D. Knolle, H.E. Jolin, E.M. Serrao, L. Haim-Vilmovsky, S.A. Teichmann, H.R. Rodewald, et al. 2018. Tissue-restricted adaptive type 2 immunity is orchestrated by expression of the costimulatory molecule OX40L on group 2 innate lymphoid cells. *Immunity*. 48:1195–1207.e6. https://doi.org/10.1016/j.immuni.2018.05.003

Hanukoglu, I., and A. Hanukoglu. 2016. Epithelial sodium channel (ENaC) family: Phylogeny, structure-function, tissue distribution, and associated inherited diseases. *Gene*. 579:95–132. https://doi.org/10.1016/j.gene.2015.12.061

Howard, E., B.P. Hurrell, D.G. Helou, P. Shafiei-Jahani, S. Hasiakos, J. Painter, S. Srikanth, Y. Gwack, and O. Akbari. 2023. Orai inhibition modulates pulmonary ILC2 metabolism and alleviates airway hyperreactivity in murine and humanized models. *Nat. Commun.* 14:5989. https://doi.org/10.1038/s41467-023-41065-4

Hurrell, B.P., L. Galle-Treger, P.S. Jahani, E. Howard, D.G. Helou, H. Banie, P. Soroosh, and O. Akbari. 2019. TNFR2 signaling enhances ILC2 survival, function, and induction of airway hyperreactivity. *Cell Rep.* 29:4509–4524.e5. https://doi.org/10.1016/j.celrep.2019.11.102

Hurrell, B.P., D.G. Helou, P. Shafiei-Jahani, E. Howard, J.D. Painter, C. Quach, and O. Akbari. 2022. Cannabinoid receptor 2 engagement promotes group 2 innate lymphoid cell expansion and enhances airway hyperreactivity. *J. Allergy Clin. Immunol.* 149:1628–1642.e10. https://doi.org/10.1016/j.jaci.2021.09.037

Hurrell, B.P., P. Shafiei Jahani, and O. Akbari. 2018. Social networking of group two innate lymphoid cells in allergy and asthma. *Front. Immunol.* 9:2694. https://doi.org/10.3389/fimmu.2018.02694

Jaalouk, D.E., and J. Lammerding. 2009. Mechanotransduction gone awry. *Nat. Rev. Mol. Cell Biol.* 10:63–73. https://doi.org/10.1038/nrm2597

Jairaman, A., S. Othy, J.L. Dynes, A.V. Yeromin, A. Zavala, M.L. Greenberg, J.L. Nourse, J.R. Holt, S.M. Cahalan, F. Marangoni, et al. 2021. Piezo1 channels restrain regulatory T cells but are dispensable for effector CD4$^+$ T cell responses. *Sci. Adv.* 7:eabg5859. https://doi.org/10.1126/sciadv.abg5859

Jha, P., and H. Das. 2017. KLF2 in regulation of NF-κB-Mediated immune cell function and inflammation. *Int. J. Mol. Sci.* 18:2383. https://doi.org/10.3390/ijms18112383

Jia, Q., Y. Yang, X. Chen, S. Yao, and Z. Hu. 2022. Emerging roles of mechanosensitive ion channels in acute lung injury/acute respiratory distress syndrome. *Respir. Res.* 23:366. https://doi.org/10.1186/s12931-022-02303-3

Jia, Y., Y. Zhao, T. Kusakizako, Y. Wang, C. Pan, Y. Zhang, O. Nureki, M. Hattori, and Z. Yan. 2020. TMC1 and TMC2 proteins are pore-forming subunits of mechanosensitive ion channels. *Neuron*. 105:310–321.e3. https://doi.org/10.1016/j.neuron.2019.10.017

Kim, K.X., M. Beurg, C.M. Hackney, D.N. Furness, S. Mahendrasingam, and R. Fettiplace. 2013. The role of transmembrane channel-like proteins in the operation of hair cell mechanotransducer channels. *J. Gen. Physiol.* 142:493–505. https://doi.org/10.1085/jgp.201311068

Kumari, S., S. Curado, V. Mayya, and M.L. Dustin. 2014. T cell antigen receptor activation and actin cytoskeleton remodeling. *Biochim. Biophys. Acta*. 1838:546–556. https://doi.org/10.1016/j.bbamem.2013.05.004

Lei, A.H., Q. Xiao, G.Y. Liu, K. Shi, Q. Yang, X. Li, Y.F. Liu, H.K. Wang, W.P. Cai, Y.J. Guan, et al. 2018. ICAM-1 controls development and function of ILC2. *J. Exp. Med.* 215:2157–2174. https://doi.org/10.1084/jem.20172359

Leng, S., X. Zhang, S. Wang, J. Qin, Q. Liu, A. Liu, Z. Sheng, Q. Feng, X. Hu, and J. Peng. 2022. Ion channel Piezo1 activation promotes aerobic glycolysis in macrophages. *Front. Immunol.* 13:976482. https://doi.org/10.3389/fimmu.2022.976482

Lesage, F., and M. Lazdunski. 2000. Molecular and functional properties of two-pore-domain potassium channels. *Am. J. Physiol. Ren. Physiol.* 279:F793–F801. https://doi.org/10.1152/ajprenal.2000.279.5.F793

Li, J., B. Hou, S. Tumova, K. Muraki, A. Bruns, M.J. Ludlow, A. Sedo, A.J. Hyman, L. McKeown, R.S. Young, et al. 2014. Piezo1 integration of vascular architecture with physiological force. *Nature*. 515:279–282. https://doi.org/10.1038/nature13701

Liu, B., W.C. Ou, L. Fang, C.W. Tian, and Y. Xiong. 2023a. Myocyte enhancer factor 2A plays a central role in the regulatory networks of cellular physiopathology. *Aging Dis.* 14:331–349. https://doi.org/10.14336/AD.2022.0825

Liu, C., Y. Xia, S. Fu, F. Meng, B. Feng, L. Xu, L. Li, and X. Zuo. 2023b. Inhibition of Piezo1 ameliorates intestinal inflammation and limits the activation of group 3 innate lymphoid cells in experimental colitis. *J. Innate Immun.* 15:709–723. https://doi.org/10.1159/000533525

Ma, S., S. Cahalan, G. LaMonte, N.D. Grubaugh, W. Zeng, S.E. Murthy, E. Paytas, R. Gamini, V. Lukacs, T. Whitwam, et al. 2018. Common PIEZO1 allele in african populations causes RBC dehydration and attenuates plasmodium infection. *Cell*. 173:443–455.e12. https://doi.org/10.1016/j.cell.2018.02.047

Ma, S., A.E. Dubin, Y. Zhang, S.A.R. Mousavi, Y. Wang, A.M. Coombs, M. Loud, I. Andolfo, and A. Patapoutian. 2021. A role of PIEZO1 in iron metabolism in mice and humans. *Cell*. 184:969–982.e13. https://doi.org/10.1016/j.cell.2021.01.024

Maazi, H., N. Patel, I. Sankaranarayanan, Y. Suzuki, D. Rigas, P. Soroosh, G.J. Freeman, A.H. Sharpe, and O. Akbari. 2015. ICOS:ICOS-ligand interaction is required for type 2 innate lymphoid cell function, homeostasis, and induction of airway hyperreactivity. *Immunity*. 42:538–551. https://doi.org/10.1016/j.immuni.2015.02.007

Matsumura, F. 2005. Regulation of myosin II during cytokinesis in higher eukaryotes. *Trends Cell Biol.* 15:371–377. https://doi.org/10.1016/j.tcb.2005.05.004

Niu, N., S. Xu, Y. Xu, P.J. Little, and Z.G. Jin. 2019. Targeting mechanosensitive transcription factors in atherosclerosis. *Trends Pharmacol. Sci.* 40:253–266. https://doi.org/10.1016/j.tips.2019.02.004

Nonomura, K., V. Lukacs, D.T. Sweet, L.M. Goddard, A. Kanie, T. Whitwam, S.S. Ranade, T. Fujimori, M.L. Kahn, and A. Patapoutian. 2018. Mechanically activated ion channel PIEZO1 is required for lymphatic valve formation. *Proc. Natl. Acad. Sci. USA*. 115:12817–12822. https://doi.org/10.1073/pnas.1817070115

Pascal, M., A. Kazakov, G. Chevalier, L. Dubrule, J. Deyrat, A. Dupin, S. Saha, F. Jagot, K. Sailor, S. Dulauroy, et al. 2022. The neuropeptide VIP potentiates intestinal innate type 2 and type 3 immunity in response to feeding. *Mucosal Immunol.* 15:629–641. https://doi.org/10.1038/s41385-022-00516-9

Petrova, T., J. Pesic, K. Pardali, M. Gaestel, and J.S.C. Arthur. 2020. p38 MAPK signalling regulates cytokine production in IL-33 stimulated Type 2 Innate Lymphoid cells. *Sci. Rep.* 10:3479. https://doi.org/10.1038/s41598-020-60089-0

Pinto, S.M., R.S. Nirujogi, P.L. Rojas, A.H. Patil, S.S. Manda, Y. Subbannayya, J.C. Roa, A. Chatterjee, T.S. Prasad, and A. Pandey. 2015. Quantitative phosphoproteomic analysis of IL-33-mediated signaling. *Proteomics*. 15:532–544. https://doi.org/10.1002/pmic.201400303

Pinto, S.M., Y. Subbannayya, D.A.B. Rex, R. Raju, O. Chatterjee, J. Advani, A. Radhakrishnan, T.S. Keshava Prasad, M.R. Wani, and A. Pandey. 2018. A network map of IL-33 signaling pathway. *J. Cell Commun. Signal.* 12:615–624. https://doi.org/10.1007/s12079-018-0464-4

Retailleau, K., F. Duprat, M. Arhatte, S.S. Ranade, R. Peyronnet, J.R. Martins, M. Jodar, C. Moro, S. Offermanns, Y. Feng, et al. 2015. Piezo1 in smooth muscle cells is involved in hypertension-dependent arterial remodeling. *Cell Rep.* 13:1161–1171. https://doi.org/10.1016/j.celrep.2015.09.072

Salo, P.M., S.J. Arbes Jr., M. Sever, R. Jaramillo, R.D. Cohn, S.J. London, and D.C. Zeldin. 2006. Exposure to Alternaria alternata in US homes is associated with asthma symptoms. *J. Allergy Clin. Immunol.* 118:892–898. https://doi.org/10.1016/j.jaci.2006.07.037

Samanta, A., T.E.T. Hughes, and V.Y. Moiseenkova-Bell. 2018. Transient receptor potential (TRP) channels. *Subcell. Biochem.* 87:141–165. https://doi.org/10.1007/978-981-10-7757-9_6

Saotome, K., S.E. Murthy, J.M. Kefauver, T. Whitwam, A. Patapoutian, and A.B. Ward. 2018. Structure of the mechanically activated ion channel Piezo1. *Nature*. 554:481–486. https://doi.org/10.1038/nature25453

Sato, Y., S. Tansho-Nagakawa, T. Ubagai, and Y. Ono. 2020. Analysis of immune responses in Acinetobacter baumannii-infected klotho knockout mice: A mouse model of Acinetobacter baumannii infection in aged hosts. *Front. Immunol.* 11:601614. https://doi.org/10.3389/fimmu.2020.601614

Snelgrove, R.J., L.G. Gregory, T. Peiró, S. Akthar, G.A. Campbell, S.A. Walker, and C.M. Lloyd. 2014. Alternaria-derived serine protease activity drives IL-33-mediated asthma exacerbations. *J. Allergy Clin. Immunol.* 134:583–592.e6. https://doi.org/10.1016/j.jaci.2014.02.002

Solis, A.G., P. Bielecki, H.R. Steach, L. Sharma, C.C.D. Harman, S. Yun, M.R. de Zoete, J.N. Warnock, S.D.F. To, A.G. York, et al. 2019. Mechanosensation of cyclical force by PIEZO1 is essential for innate immunity. *Nature*. 573:69–74. https://doi.org/10.1038/s41586-019-1485-8

Spits, H., and J. Mjösberg. 2022. Heterogeneity of type 2 innate lymphoid cells. *Nat. Rev. Immunol.* 22:701–712. https://doi.org/10.1038/s41577-022-00704-5

Syeda, R., J. Xu, A.E. Dubin, B. Coste, J. Mathur, T. Huynh, J. Matzen, J. Lao, D.C. Tully, I.H. Engels, et al. 2015. Chemical activation of the mechanotransduction channel Piezo1. *Elife*. 4:e07369. https://doi.org/10.7554/eLife.07369

Tang, Y., C. Zhao, Y. Zhuang, A. Zhong, M. Wang, W. Zhang, and L. Zhu. 2023. Mechanosensitive Piezo1 protein as a novel regulator in macrophages and macrophage-mediated inflammatory diseases. *Front. Immunol.* 14:1149336. https://doi.org/10.3389/fimmu.2023.1149336

Turpaev, K.T. 2020. Transcription factor KLF2 and its role in the regulation of inflammatory processes. *Biochemistry*. 85:54–67. https://doi.org/10.1134/S0006297920010058

Vicente-Manzanares, M., X. Ma, R.S. Adelstein, and A.R. Horwitz. 2009. Nonmuscle myosin II takes centre stage in cell adhesion and migration. *Nat. Rev. Mol. Cell Biol.* 10:778–790. https://doi.org/10.1038/nrm2786

Vivier, E., D. Artis, M. Colonna, A. Diefenbach, J.P. Di Santo, G. Eberl, S. Koyasu, R.M. Locksley, A.N.J. McKenzie, R.E. Mebius, et al. 2018. Innate lymphoid cells: 10 Years on. *Cell*. 174:1054–1066. https://doi.org/10.1016/j.cell.2018.07.017

Wallrapp, A., S.J. Riesenfeld, P.R. Burkett, R.E. Abdulnour, J. Nyman, D. Dionne, M. Hofree, M.S. Cuoco, C. Rodman, D. Farouq, et al. 2017. The neuropeptide NMU amplifies ILC2-driven allergic lung inflammation. *Nature*. 549:351–356. https://doi.org/10.1038/nature24029

Wang, Y., H. Yang, A. Jia, Y. Wang, Q. Yang, Y. Dong, Y. Hou, Y. Cao, L. Dong, Y. Bi, and G. Liu. 2022. Dendritic cell Piezo1 directs the differentiation of T_H1 and T_{reg} cells in cancer. *Elife*. 11:e79957. https://doi.org/10.7554/eLife.79957

Weber, J., S. Rajan, C. Schremmer, Y.K. Chao, G. Krasteva-Christ, M. Kannler, A.Ö. Yildirim, M. Brosien, J. Schredelseker, N. Weissmann, et al. 2020. TRPV4 channels are essential for alveolar epithelial barrier function as protection from lung edema. *JCI Insight*. 5:e134464. https://doi.org/10.1172/jci.insight.134464

Wilhelm, C., O.J. Harrison, V. Schmitt, M. Pelletier, S.P. Spencer, J.F. Urban Jr., M. Ploch, T.R. Ramalingam, R.M. Siegel, and Y. Belkaid. 2016. Critical role of fatty acid metabolism in ILC2-mediated barrier protection during malnutrition and helminth infection. *J. Exp. Med.* 213:1409–1418. https://doi.org/10.1084/jem.20151448

Woo, S.H., V. Lukacs, J.C. de Nooij, D. Zaytseva, C.R. Criddle, A. Francisco, T.M. Jessell, K.A. Wilkinson, and A. Patapoutian. 2015. Piezo2 is the principal mechanotransduction channel for proprioception. *Nat. Neurosci.* 18:1756–1762. https://doi.org/10.1038/nn.4162

Xu, M., C. Li, J. Yang, A. Ye, L. Yan, B.S. Yeoh, L. Shi, Y.S. Kim, J. Kang, M. Vijay-Kumar, and N. Xiong. 2022. Activation of $CD81^+$ skin ILC2s by cold-sensing $TRPM8^+$ neuron-derived signals maintains cutaneous thermal homeostasis. *Sci. Immunol.* 7:eabe0584. https://doi.org/10.1126/sciimmunol.abe0584

Xu, Y., S. Xu, P. Liu, M. Koroleva, S. Zhang, S. Si, and Z.G. Jin. 2017. Suberanilohydroxamic acid as a pharmacological kruppel-like factor 2 activator that represses vascular inflammation and atherosclerosis. *J. Am. Heart Assoc.* 6:e007134. https://doi.org/10.1161/JAHA.117.007134

Yoneda, M., H. Suzuki, N. Hatano, S. Nakano, Y. Muraki, K. Miyazawa, S. Goto, and K. Muraki. 2019. PIEZO1 and TRPV4, which are distinct mechano-sensors in the osteoblastic MC3T3-E1 cells, modify cell-proliferation. *Int. J. Mol. Sci.* 20:4960. https://doi.org/10.3390/ijms20194960

Zhang, M., Y. Wang, J. Geng, S. Zhou, and B. Xiao. 2019. Mechanically activated piezo channels mediate touch and suppress acute mechanical pain response in mice. *Cell Rep.* 26:1419–1431.e4. https://doi.org/10.1016/j.celrep.2019.01.056

Zheng, Q., Y. Zou, P. Teng, Z. Chen, Y. Wu, X. Dai, X. Li, Z. Hu, S. Wu, Y. Xu, et al. 2022. Mechanosensitive channel PIEZO1 senses shear force to induce KLF2/4 expression via CaMKII/MEKK3/ERK5 Axis in endothelial cells. *Cells*. 11:2191. https://doi.org/10.3390/cells11142191

Zhou, F., X. Xu, J. Wu, D. Wang, and J. Wang. 2017. NF-κB controls four genes encoding core enzymes of tricarboxylic acid cycle. *Gene*. 621:12–20. https://doi.org/10.1016/j.gene.2017.04.012

Supplemental material

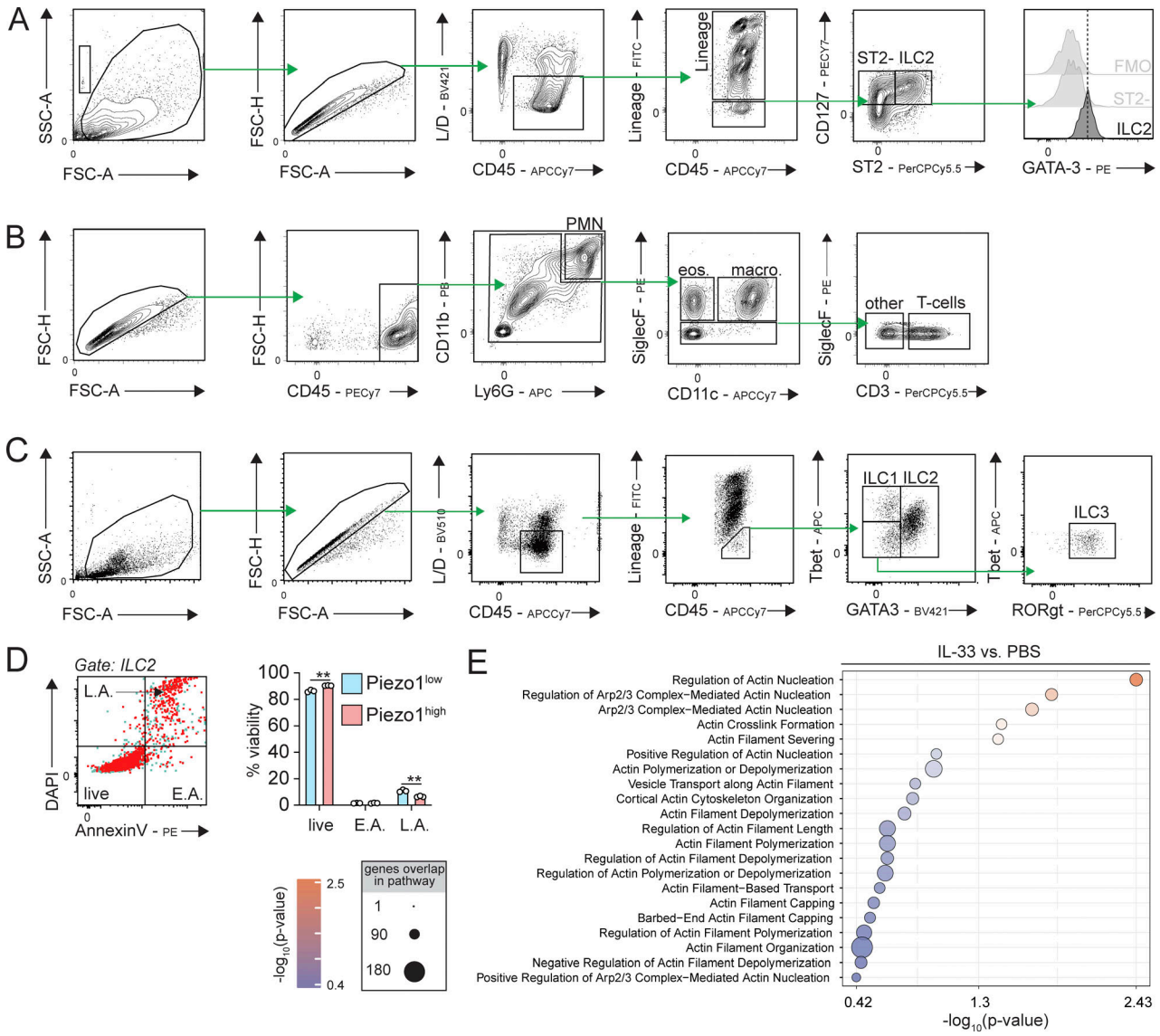

Figure S1. **Gating strategies and viability of Piezo1^{high} and Piezo1^{low} ILC2s. (A and B)** ILC2 gating strategy (A) and myeloid cell/T cell gating strategy (B). **(C)** Gating strategy used for the intranuclear staining of ILC1, ILC2, and ILC3. **(D)** Representative plots of live, early apoptotic (E.A.), and late apoptotic/necrotic (L.A.) ILC2s and corresponding quantitation presented as the frequencies (%) of live, E.A., and L.A. ILC2s. *n* = 3. The experiment was performed twice. **(E)** Pure populations of lung ILC2s were FACS-sorted from mice challenged with either PBS or IL-33 and profiled by droplet-based scRNA-seq (Wallrapp et al., 2017). Gene set enrichment analysis performed by IPA depicting top actin remodeling pathways induced by IL-33 treatment in murine lung ILC2s. All pathways shown are enriched in IL-33–treated ILC2s compared with PBS-treated ILC2s. The size of the dots represents the number of gene overlaps in each pathway, colors indicated P value. Data are presented as mean ± SEM. A two-tailed Student's *t* test for unpaired data was applied for comparisons between two groups (D). **P < 0.01.

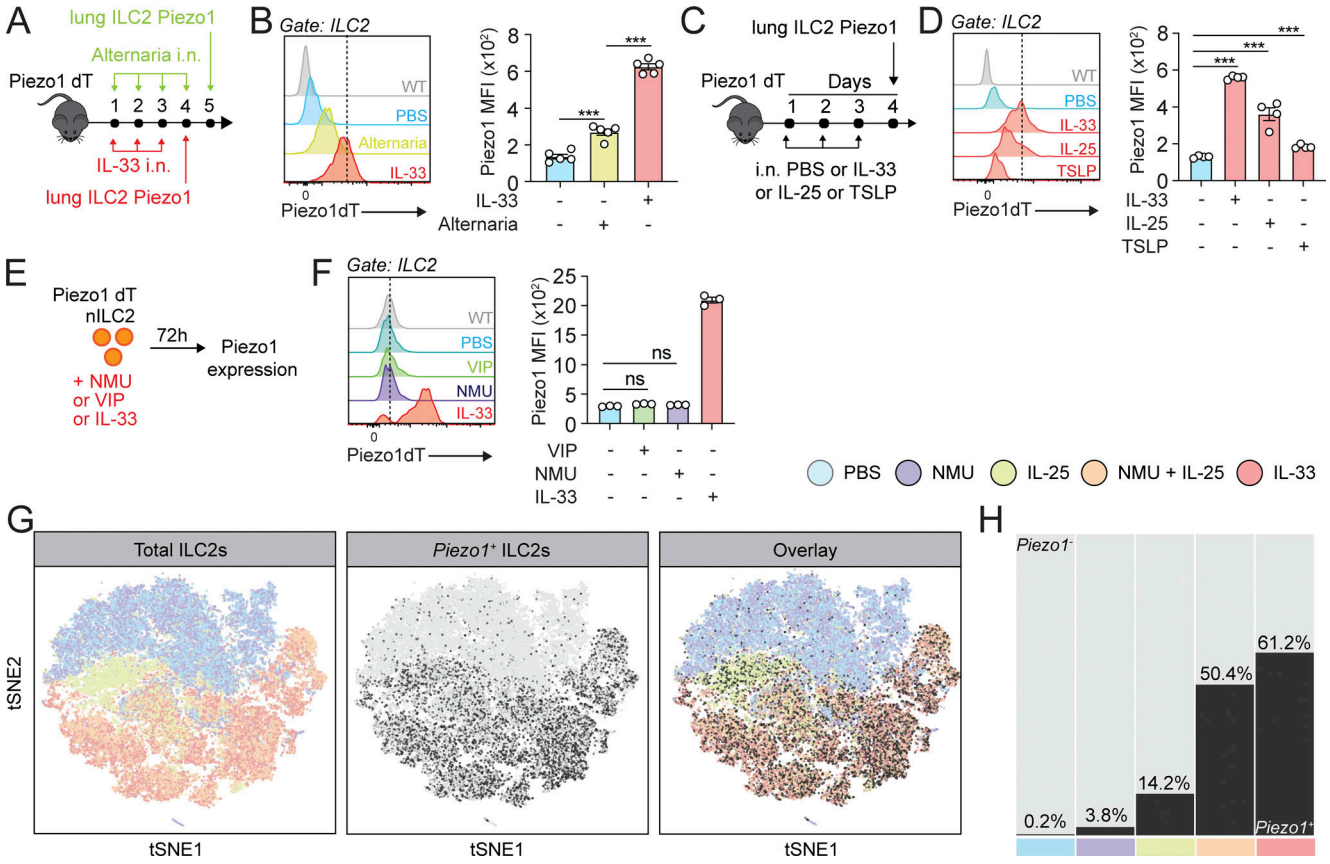

Figure S2. **Effects of IL-33, IL-25, TSLP, NMU, and VIP on ILC2 Piezo1 expression. (A)** Cohorts of Piezo1dT mice were challenged i.n. for 3 consecutive days (0.5 µg rmIL-33) or 4 consecutive days (100 µg *A. Alternata*). Cohorts of mice challenged with PBS were used as controls. The expression of Piezo1 in lung ILC2s was measured 24 h after the last intranasal challenge by flow cytometry. **(B)** Representative flow cytometry plots of Piezo1 expression and corresponding quantitation, presented as Piezo1dT MFI. *n* = 5. The experiment was performed three times. **(C)** Cohorts of Piezo1dT mice were challenged i.n. for 3 consecutive days with either rmIL-33, rmIL-25, or rmTSLP (all 0.5 µg/mouse). Cohorts of mice challenged with PBS were used as controls. The expression of Piezo1 in lung ILC2s was measured 24 h after the last intranasal challenge by flow cytometry. **(D)** Representative flow cytometry plots of Piezo1 expression and corresponding quantitation, presented as Piezo1dT MFI. *n* = 5. The experiment was performed three times. **(E)** Schematic description of ex vivo lung ILC2 Piezo1 analysis. Pure populations of naïve ILC2s were FACS-sorted from the lungs of Piezo1dT mice and cultured ex vivo with rmIL-2 and rmIL-7 (both 10 ng/ml) for the indicated times with or without rmIL-33 (20 ng/ml), VIP (10 µM), or NMU (100 ng/ml) for 72 h. **(F)** Representative flow cytometry plots of Piezo1 expression and corresponding quantitation, presented as Piezo1dT MFI. *n* = 3. The experiment was performed twice. **(G)** Pure populations of lung ILC2s were FACS-sorted from mice challenged with either PBS, IL-33, IL-25, NMU, or NMU+IL-25 and profiled by droplet-based scRNA-seq (Wallrapp et al., 2017). Cells (dots) are colored based on in vivo treatment, either PBS (blue) or IL-33 (red), NMU (purple), IL-25 (green), and NMU+IL-25 (orange). tSNE1 projections showing total ILC2s (left panel) and *Piezo1*⁺ ILC2s (middle panel) and an overlay (right panel). **(H)** Frequencies of Piezo1⁺ cells in each experimental condition. Data are presented as mean ± SEM. Tukey's multiple comparison one-way ANOVA tests were used (B, D, and F). ***P < 0.001, ns: non-significant.

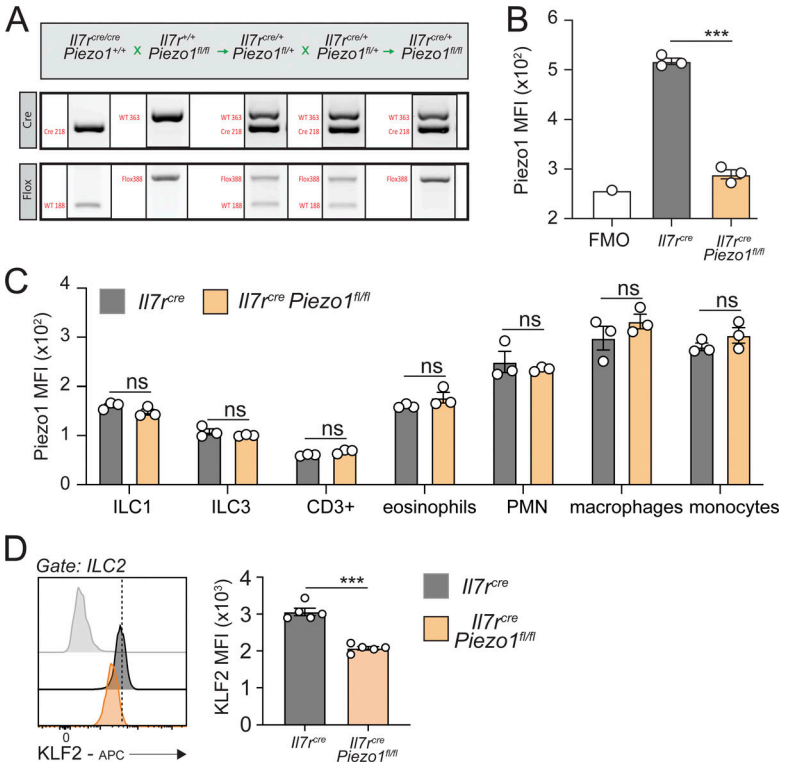

Figure S3. **Generation and validation of *Il7r^{cre} Piezo1$^{fl/fl}$* mice. (A)** Representative bands from DNA gels for genotyping and generation of *Il7r^{cre}Piezo1$^{fl/fl}$* mice. **(B)** *Il7r^{cre}* and *Il7r^{cre} Piezo1$^{fl/fl}$* mice were i.n. challenged on days 1–3 with 0.5 µg IL-33. On day 4, lungs were processed to single-cell suspensions and stained for ILC2s and Piezo1. Piezo1 MFI. *n* = 3. The experiment was performed twice. **(C)** Piezo1 expression in indicated ILC, T cell, and myeloid populations isolated from the lungs of *Il7r^{cre}* and *Il7r^{cre}Piezo1$^{fl/fl}$* mice. *n* = 3. The experiment was performed twice. **(D)** Representative flow cytometry plots of ILC2 intranuclear KLF2 expression and quantitation presented as KLF2 MFI. *n* = 5. The experiment was performed twice. Data are presented as mean ± SEM. A two-tailed Student's *t* test for unpaired data was applied for comparisons between two groups (B–D). ***P < 0.001. ns: non-significant. Source data are available for this figure: SourceData FS3.

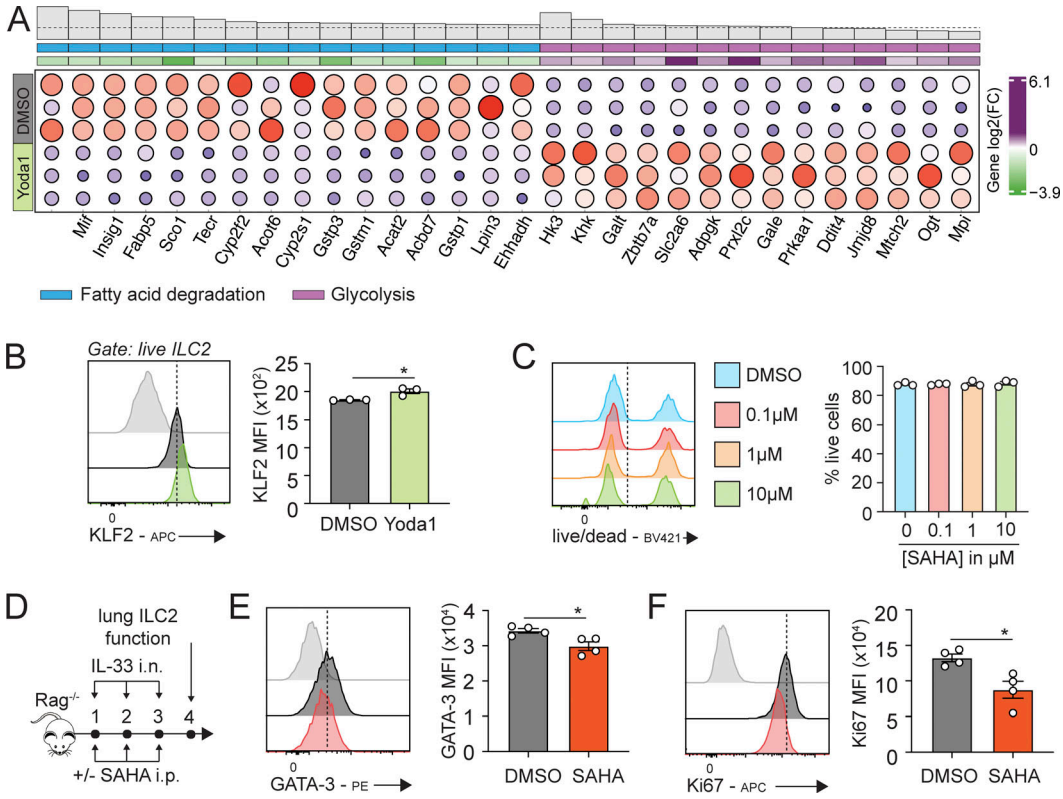

Figure S4. **Effects of Yoda1 and SAHA on ILC2s. (A–C)** BALB/c mice were challenged i.n. on 3 consecutive days with rmIL-33, and a pure population of lung ILC2s was isolated on day 4 and cultured with rmIL-2, rmIL-7 without or with (A and B) Yoda1 (10 μM) or (C) increasing doses of SAHA for 18 h. **(A)** Cells were collected, and RNA was extracted to perform a bulk transcriptomic analysis. Dot plot representation depicting fatty acid degradation and glycolysis gene signatures in Yoda1 or control-treated ILC2s. **(B)** Representative dot plots of ILC2 intranuclear KLF2 expression and corresponding quantitation presented as KLF2 MFI. *n* = 3. The experiment was performed twice. **(C)** Frequencies of live cells in response to increasing doses of SAHA analyzed using the live/dead stain after 18 h of culture. *n* = 4. The experiment was performed twice. **(D)** Schematic description of in vivo SAHA administration. *Rag2*$^{-/-}$ mice received intraperitoneal injections of 100 mg/kg SAHA or vehicle control and 0.5 μg rmIL-33 or PBS i.n. on days 1–3. On day 4, lung ILC2s were analyzed. The experiment was performed twice. **(E and F)** Representative plots of intranuclear (E) GATA-3 and (F) Ki67 expressions and corresponding quantitation are presented as MFI. *n* = 4. Data are presented as mean ± SEM. A two-tailed Student's *t* test for unpaired data was applied for comparisons between two groups (B, E, and F). *P < 0.05.

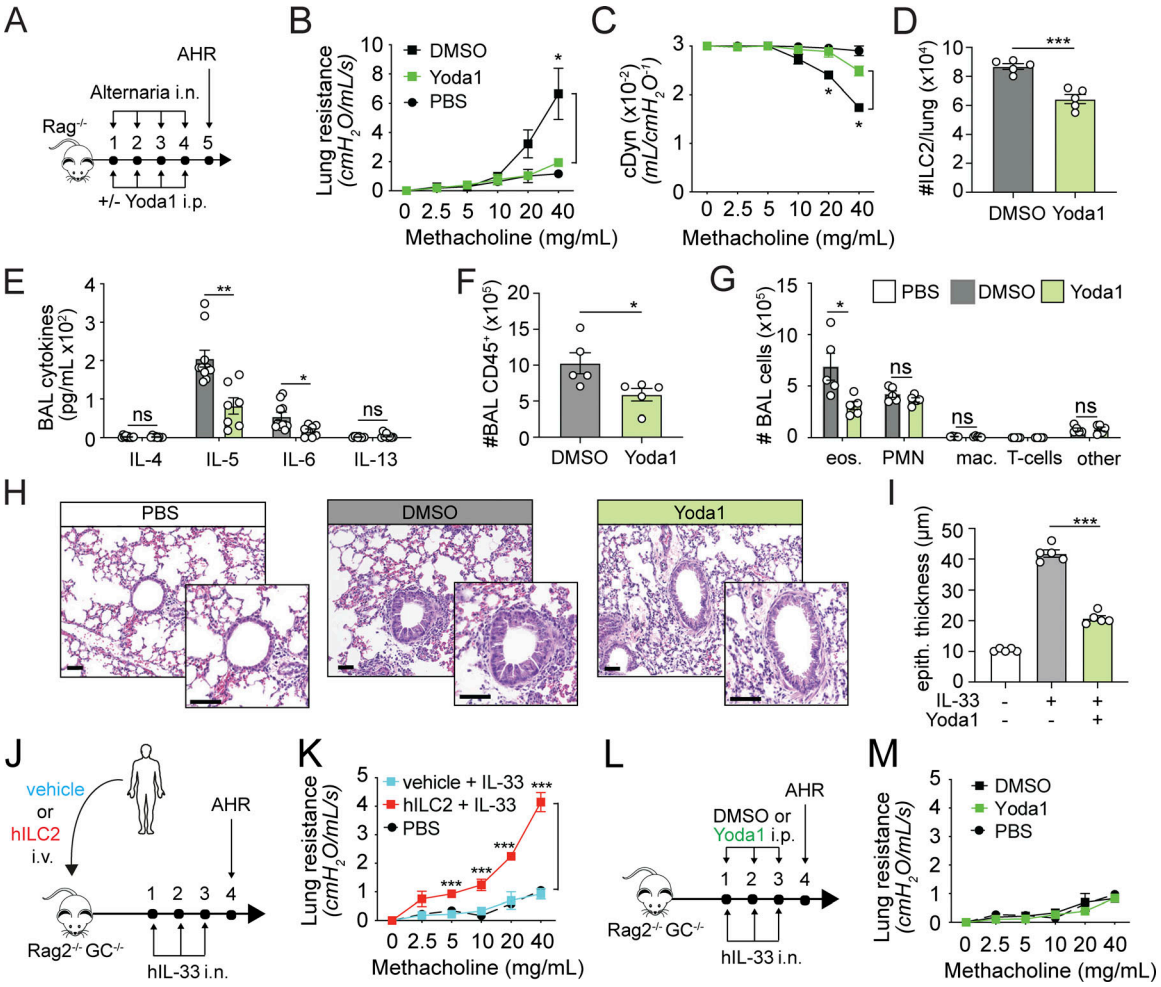

Figure S5. **In vivo Yoda1 treatment reduces AHR and lung inflammation after *A. alternata* challenge. (A)** Schematic description of in vivo effects of Piezo1 activation on the development of AHR. *Rag2*$^{-/-}$ mice received intraperitoneal injections of 213 µg/kg/day Yoda1 or vehicle control and 100 µg *A. Alternata* or PBS i.n. on days 1–4. On day 5, lung function, lung ILC2s, BAL cellularity, and histology were analyzed. The experiment was performed twice. **(B and C)** Lung resistance (B) and dynamic compliance (C) in response to increasing doses of methacholine. *n* = 5. **(D)** Total number of ILC2s per lung. *n* = 5. **(E)** Levels of IL-4, IL-5, IL-6, and IL-13 in the BAL. *n* = 8. **(F)** Total number of CD45$^+$ lymphoid cells in the BAL. *n* = 5. **(G)** Numbers of BAL eosinophils (CD45$^+$, CD11c$^-$, SiglecF$^+$), neutrophils (PMN, CD45$^+$, SiglecF$^-$, Ly6G$^+$, CD11b$^+$), macrophages (CD45$^+$, Ly6G$^-$, SiglecF$^-$, CD11c$^+$), T cells (CD45$^+$, CD3$^+$), and others. *n* = 5. **(H)** Lung histology. Scale bars, 50 µm. **(I)** Average alveolar epithelial thickness. *n* = 5. **(J)** Schematic representation of the induction of airway inflammation by adoptively transferred human donor ILC2s in alymphoid recipients. PBMCs were isolated from 500 ml of blood from healthy subjects. After isolation of CD45$^+$ Lineage$^-$ CRTH2$^+$ CD127$^+$ hILC2s, cells were cultured (5 × 10^5/ml) in rhIL-2, rhIL-7, (both 20 ng/ml) and decreasing doses of rhIL-33 (100, 50, 25, and 10 ng/ml) every 72 h or until the required number of cells was achieved. 1 × 10^5 human donor ILC2s or vehicle were then subsequently transferred intravenously to *Rag2*$^{-/-}$*GC*$^{-/-}$ recipient mice, who then received 0.5 µg rmIL-33 i.n. on days 1–3. On day 4, lung function was analyzed. The experiment was performed twice. **(K)** Lung resistance in response to increasing doses of methacholine. *n* = 3. **(L)** Cohorts of *Rag2*$^{-/-}$*GC*$^{-/-}$ mice received intraperitoneal injections of 213 µg/kg/day Yoda1 or vehicle control and 0.5 µg hIL-33 i.n. on days 1–3. On day 4, lung function was analyzed. The experiment was performed twice. **(M)** Lung resistance in response to increasing doses of methacholine. *n* = 3. Data are presented as mean ± SEM. A two-tailed Student's *t* test for unpaired data was applied for comparisons between two groups (D–G), except for multigroup comparisons where Tukey's multiple comparison one-way ANOVA tests were used (B, C, and I). *P < 0.05, **P < 0.01, ***P < 0.001. ns: non-significant.